UNIVERSITY OF THE PHILIPPINES

Master of Science in Environmental Engineering

**CELSO M. ISIDRO**

# Remote Detection of Placer Deposits and Iron-bearing Minerals using the Infrared Spectrum for the Identification of Environmental Monitoring Sites in Benguet Catchment

Thesis Adviser:

**HERMAN D. MENDOZA, Dr. Eng.**
Department of Mining, Metallurgical and Materials Engineering
University of the Philippines Diliman

Date of Submission

May 2018

Thesis Classification

**F**

This thesis is available for public.

# REMOTE DETECTION OF PLACER DEPOSITS AND IRON-BEARING MINERALS USING THE INFRARED SPECTRUM FOR THE IDENTIFICATION OF ENVIRONMENTAL MONITORING SITES IN BENGUET CATCHMENT

**Thesis by**

**Celso Isidro**
**BS in Mining Engineering**

**Submitted to the National Graduate School of Engineering**
**College of Engineering**
**University of the Philippines**

**In Partial Fulfillment of the Requirements**
**For the Degree of Master of Science**
**Environmental Engineering**

**National Graduate School of Engineering**
**College of Engineering**
**University of the Philippines, Diliman**
**Quezon City**

**May 2018**

This thesis, entitled **REMOTE DETECTION OF PLACER DEPOSITS AND IRON-BEARING MINERALS USING THE INFRARED SPECTRUM FOR THE IDENTIFICATION OF ENVIRONMENTAL MONITORING SITES IN BENGUET CATCHMENT,** prepared and submitted by **CELSO M. ISIDRO**, in partial fulfilment of the requirements for the degree of **M.S. ENVIRONMENTAL ENGINEERING** is hereby accepted.

**HERMAN D. MENDOZA, Dr. Eng.**
Thesis Adviser

Accepted as partial fulfilment of the requirements for the degree **M.S. ENVIRONMENTAL ENGINEERING**.

**RIZALINDA L. DE LEON, Ph.D.**
Dean

# ACKNOWLEDGMENT

This research would not be possible without the guidance of Prof. Herman Mendoza. Through this research project, I was able to develop my remote sensing competence, and discover the technology's extensibilities to environmental monitoring and minerals industry.

I also would like to thank Miners Project B for the provision of field data and acquisition of water quality data from third parties such as the Environmental Management Bureau (EMB). I also would like to acknowledge Planet Team for the provision of very high-resolution satellite images of RapidEye, which were useful during verification process of the research as well as to PCI Geomatics for the trial version of its remote sensing software.

This research project would not be possible without the continuous moral support of Donamae Isidro, my loving wife. Lastly, to God who never stops on providing me spiritual growth to achieve my purpose, to Him be the glory.

# ABSTRACT OF THESIS

This study aims to investigate, using infrared spectrum the remote detection of placer deposits and their zone of mineral concentrations to identify environmental monitoring sites. The Modified Normalized Difference Water Index (MNDWI) completely separated placer deposits from river networks and lakes. It was observed that water areas highly absorbed shortwave infrared light from 1.57 μm to 1.65 μm of Landsat-8 OLI sensor, which resulted in positive MNDW index values. Whereas placer deposits reflected shortwave infrared light, and negative MNDW index was generated over these areas. In contrast, the application of Ferrous Minerals Ratio (FMR) index presented that iron-bearing minerals were separable from other placer materials due to their higher reflectance at shortwave infrared region. During rainy season, mudflow induced by rain covered placer materials near the discharge outlets whereas turbid water washed-out placer materials at higher elevations. Turbid water and mudflow resulted in spectral signatures that have low reflectance at shortwave infrared, but high reflectance at near-infrared region compared. This phenomenon reduced detected placer deposits area coverage of 2 $km^2$ and 3.7 $km^2$ for 2014 and 2015, respectively. An inverse linear relationship was generated between MNDWI and surface temperature, with an $R^2$ value of 70%. In addition, washed-out iron-bearing minerals were continuously replenished every dry season. They were detected as additional area coverage during the 1st and 2nd quarters which ranges from 0.1 $km^2$ to 1.7 $km^2$.

**Keywords:** placer deposits, modified normalized difference water index, ferrous mineral ratio, remote sensing, infrared spectrum, water quality monitoring

# TABLE OF CONTENTS

# LIST OF FIGURES

# LIST OF TABLES

# 1. INTRODUCTION

## 1.1 Background

Mineral-bearing rocks are potential host of precious metals and non-metallic commodities, which can be mined at a profit (Haneberg et al., 2014). These minerals are found either above or below ground surface level depending on the nature of geologic deposition. In addition, minerals are naturally exposed to surface through interaction of various environmental factors. Among these environmental factors, weathering performs an important role particularly in developing a placer deposit. A placer deposit is described as natural aggregation of minerals from weathered rocks (Gujar, 2007). These mineralized rocks called veins protrude on the slopes of several mountains and are exposed to chemical and mechanical weathering (Cronan, 1980). Afterwards, coarse minerals are detached and transported downslope by gravity. The rate of weathering, specifically in wet tropical regions, is influenced by humidity, rainfall rate and temperature (Plumlee, 1999). In addition, the rate of transportation, a weathering element, is augmented during high rainfall rate and air flow, which initially form an eluvial placer along hillside (Hosch, 2006). According to Harraz, 2013, these minerals can accumulate along point bars. Unless the river has very high flow rate, minerals are also buried in potholes, river channel constriction, confluences, meander loops and old stream channels (**Figure 1-1**). Moreover, the nature of deposition is controlled by bed configuration, grain density and source rock. Those minerals with heavy metals remain undisturbed on nearby sections of the river, and they form the placer deposit. In addition, heavy metals of interest in placer deposits include gold, silver, platinum, iron, chromite and tin (Harraz, 2013). In shallow

areas, they are normally extracted by different methods as follows; open-pit mining for iron deposits, hydraulicking for gold sediments and amalgamation (e.g. application of mercury, Hg) for gold concentrates in hard rocks, alluvial mining for diamonds, and manual rock breaking for tin deposits (Cronan, 1980; Luethje et al., 2014). In contrast, placer deposit is also a principal source of construction materials. In deep sea level, these non-metallic minerals are recovered by dredging.

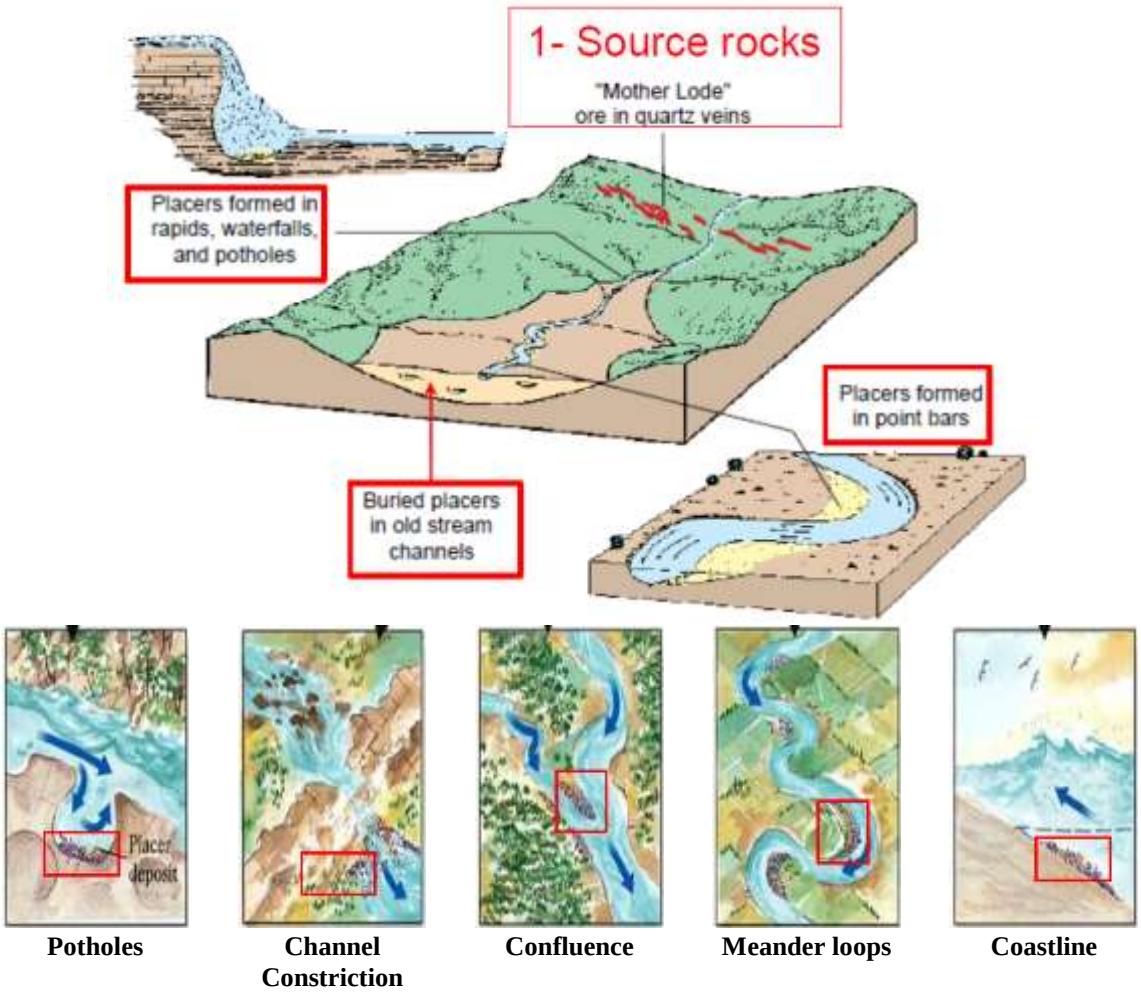


**Figure 1-1.** Placer deposit and different forms of deposition
Adapted from *Placer Mine Deposits* (p.4,21), by H. Harraz, 2013

Furthermore, placer deposit is a region known for anthropogenic activities such as quarrying and small-scale mining. Small-scale mining can involve rudimentary techniques of recovering valuable minerals (Isidro et al., 2017). In the Philippines, small-scale mining can be artisanal by nature or uses supplementary chemicals (Maglambayan et al., 2005). In developing countries, such as the Philippines, small-scale mining is typically found in regions with gold, chromite and iron deposits. For gold deposits, traditional methods of gold recovery like panning, and application of sluice boxes are being utilized in Cagayan Valley in Region II (Isidro et al., 2017). In contrast, other small-scale mines prefer using chemically-driven ore recovery techniques such as amalgamation and cyanidation for higher gold recovery. Recognized mining districts in the Philippines that adapt such techniques include the area of Agusan River basin in eastern Mindanao (Appleton, et al., 1999) and Benguet in northwest Luzon (Maglambayan, et al., 2005). Although small-scale mining of gold is being regulated in the Philippines through the Mining Law, problems on prohibited disposal of mine and mill waste to rivers remain uncontrollable. This problem can cause several impacts to river, and can augment its acidity and heavy metal content, and can introduce contamination from reagent residuals that come from ore beneficiation processes (Ghose & Sen, 1999). Likewise, heavy metals are being absorbed by plants located downstream of the river, which can also have harmful impacts to their growth (Abdul-Wahab & Marikar, 2011).

This research investigated the use of remote sensing indices in detecting the presence of placer gold deposits in Benguet province. The case study has a particular level of interest as placer deposits influence the distribution of settlers and migrants in the

province (Maglambayan et al., 2005). Since the 16th century, settlers and migrants are being found near the Benguet gold placer deposit to perform artisanal and small-scale mining. Between the years 2014 and 2015, water quality data from selected sections of Benguet catchment were collected by Environmental Management Bureau (EMB), Cordillera Administrative Region and Miners Project B funded by the Department of Science and Technology (DOST). These water quality data were used as baseline information to determine the relationship between selected water quality parameters such as Hg concentration and total suspended solids (TSS) against the detected spatial attributes of river sections potential for placer deposition. It would be worthwhile to examine the extensibility of remote sensing indices on generating an effective water quality monitoring plan with spatial and temporal dimensions. Remote sensing is an alternative to in-situ water quality monitoring and ground survey, which is more expensive, time-consuming and spatially limited (Kiefer et al., 2015). Remote sensing can offer rapid results that can be performed on a repetitive basis (Behnam et al., 2016).

## 1.2 Description of Study Area

### 1.2.1 Regional location

The Benguet province is located northwest of Luzon, and it is within the territorial boundary of Cordillera Administrative Region (CAR). It has an overall area of 2,641 $km^2$, which is comprised of Municipalities of Mankayan, Kabayan, Itogon and Virac. The province is situated on a mountainous region sitting over 1,000 meters above sea level (MASL) (**Figure 1-2**). In contrast, the Benguet catchment has an area coverage of 988 $km^2$ only, which traverses Agno and Bued rivers. The catchment is made of 30 sub-drainage basins and serve as water source to local communities (**Figure 1-2A**). In addition, the catchment has two discharge outlets (e.g delta). From north, the Ambuklao Lake is the initial river discharge outlet with a size of 1.75 $km^2$. The water from the lake flows down the Agno River, and its water is being discharged at Binga Lake with a size of 1.30 $km^2$. Moreover, the catchment rivers are classified as Class C to D. These rivers are not drinkable and are only used for industrial applications (Lubrica, 2013). For Class D rivers, the acceptable mercury (Hg) concentration is from 5 μg/L to 8 μg/L whereas total suspended solids (TSS) is from 100 mg/L to 150 mg/L.

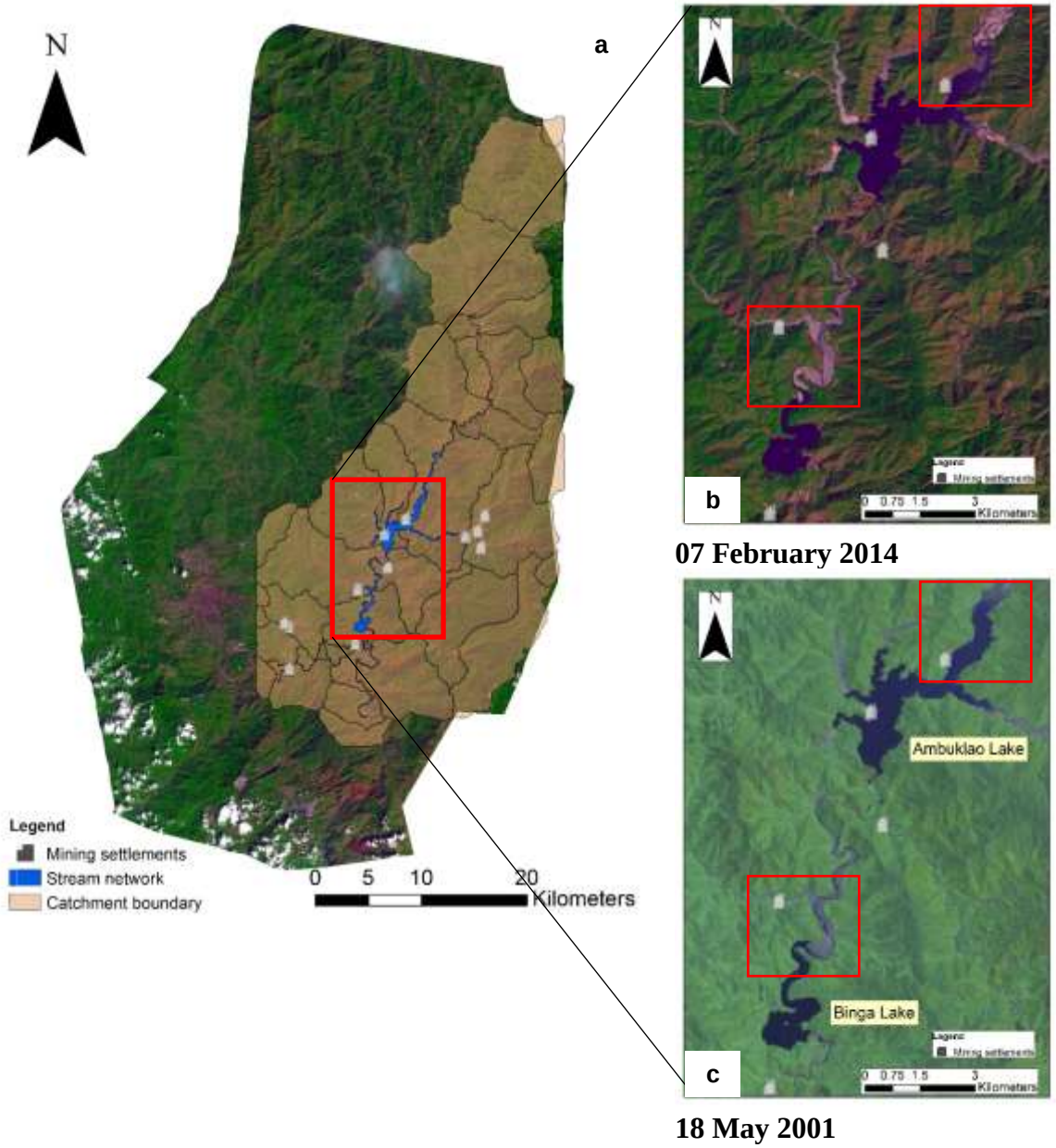


**Figure 1-2.** Hydrology of Benguet catchment and the identified mining settlements
Note: Layer stacking using Landsat-7 ETM+ and Landsat-8 OLI sensors bands for shortwave infrared 2, near-infrared, green band
(a) Benguet catchment and mining settlements; (b) Changes in placer deposits near discharge outlets in Ambuklao and Binga lakes

**Figure 1-2A** presents the full extent of Benguet catchment that includes the Ambuklao and Binga lakes in years 2001 and 2014. The 2001 image was captured by Landsat-7 ETM+ satellite sensor whereas the 2014 image was secured through the

Landsat-8 OLI satellite sensor. Mining settlements and migrants can be found distributed within the discharge outlets of river tributaries. In **Figure 1-2B and C**, the configuration of these discharge outlets was changed within 13 years, and an increase on placer deposit coverage is observable.

### 1.2.2 Topography

The Benguet catchment is surrounded mainly of mountain ranges. Mountains with very steep slopes can be found surrounding the outer catchment while gently sloping mountains are situated on selected inner sections of its sub-drainage basins. Whereas nearly level topographies are found besides Ambuklao and Binga Lakes (Canilao, 2017). Moreover, a Digital Elevation Model (DEM) generated from Shuttle Radar Topography Mission (SRTM) was utilized to produce a contour map of the catchment (**Figure 1-3**). The contour map presents these lakes together with main sections of placer deposits rest over the elevations between 600 and 750 MASL. The steep mountains are the potential source of rock materials that form the placer deposit in the catchment as shown in **Figure 1-4**.

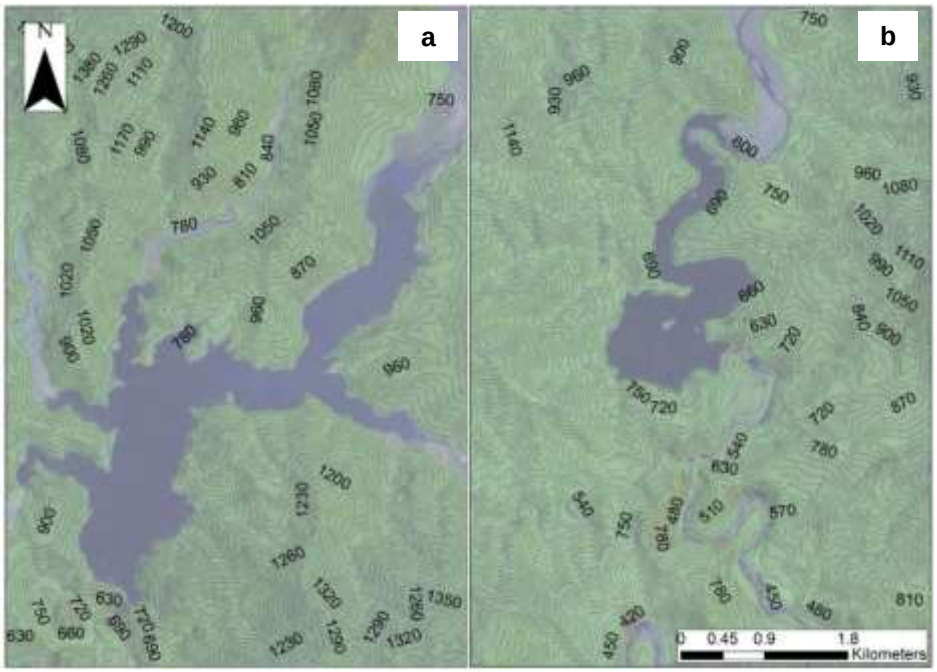


**Figure 1-3.** Contour maps of Benguet catchment surrounding areas
(a) Ambuklao Lake; (b) Binga Lake

**Figure 1-4.** Three-dimensional view of Benguet catchment
2014 RapidEye image courtesy of Planet Team (2018)

### 1.2.3 Regional climate

Benguet province has a wet tropical climate. Its location on highlands gives it a temperature lower than being experienced at sea level. Based on historical rainfall data from 2011 to 2015, average quarterly rainfall rate in the province can reach as high as 713 mm, which was recorded during the third quarter of 2015 (**Figure 1-5A**). It was concluded that the highest rainfall rates fell on the third quarter of each year. On the other hand, averaged number of days raining for each quarter presents that it is almost raining every day during the second and third quarters of each year (**Figure 1-5B**). Least occurrence of rain can be observed during the first quarter. Furthermore, it is expected that during the first quarter, mean daily rainfall rate ranges from 3 to 6 mm only whereas 11-14 mm for the second quarter, 16-24 mm for the third quarter and 5-10 mm for the fourth quarter as shown in **Figure 1-5C**.

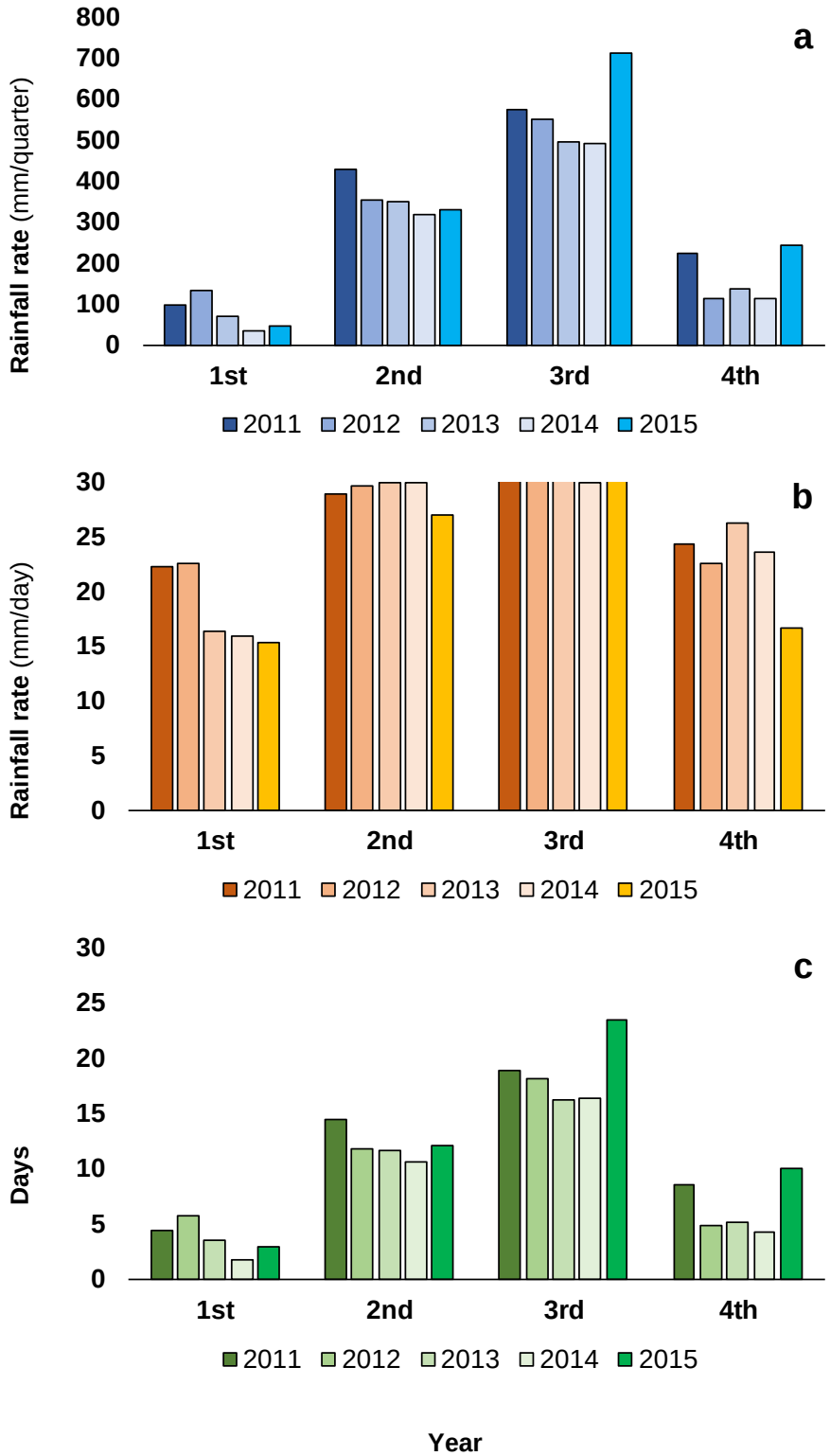


**Figure 1-5.** Recorded rainfall rate in Benguet Region between 2011 and 2015
(a) Quarterly mean rainfall rate; (b) Average days raining per quarter;
(c) Daily rainfall rate per quarter
Adapted from https://www.worldweatheronline.com/itogon-weather-averages/benguet/ph.aspx

### 1.2.4 Regional geology

The placer deposits lie over quartz diorite intrusive. This intrusive contains veins of epithermal gold deposit, which dip from northeast to southwest (Maglambayan et al., 2005). The diorite zone is highly associated with chalcopyrite, pyrite and minor amount of quartz carbonate, which are trace minerals of gold. In Benguet catchment, mineral-bearing rocks that can be found are chalcopyrite, galena, pyrite, spalerite and traces of tellurite (Fernandez & Damasco, 1979; Cooke, 1990; Worley, 1967 as cited in Maglambayan et al., 2005).

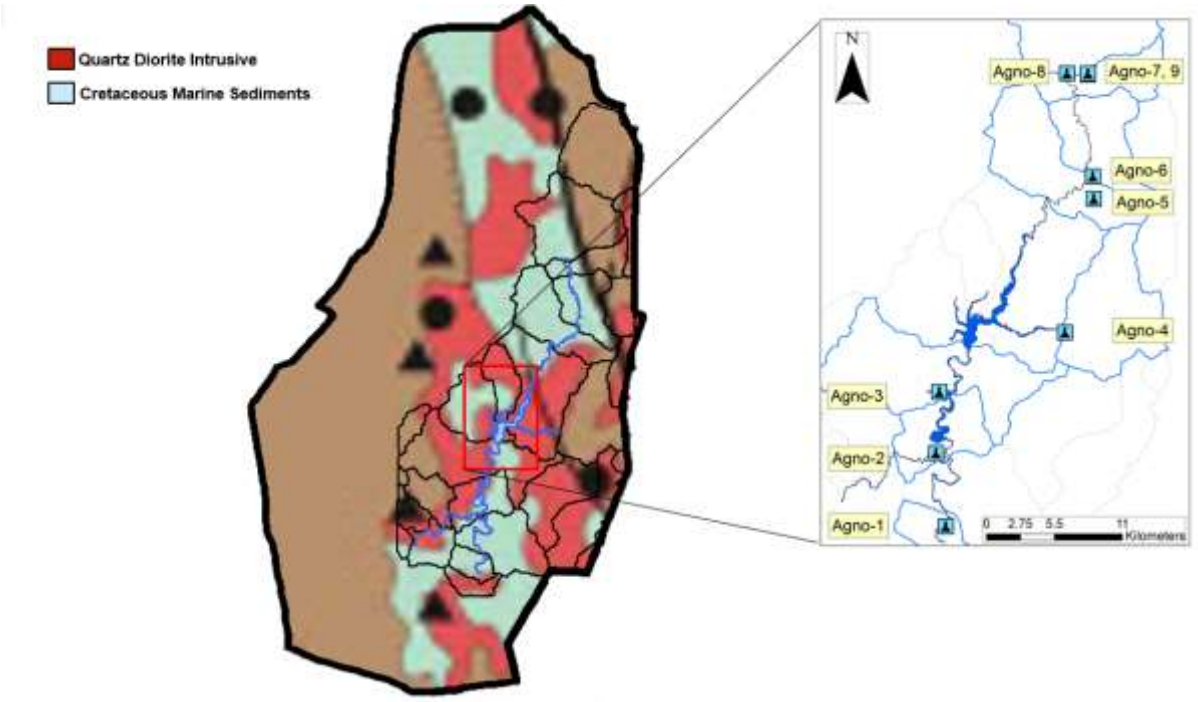


**Figure 1-6.** Regional geology of Benguet catchment
Adapted from *Technical Report for the Didipio Gold-copper Project* (p. 30), by J. McIntyre, J. Moore and J. Wyche, 2010.

### 1.2.5 Land uses

Based on previous researches, Benguet catchment is a principal concentration of established village settlements since the 18th century. These settlements were mainly induced by the presence of placer and lode gold deposits in the province (Canilao, 2017). A placer deposit is an accumulation of minerals, in this case those that contain gold concentrates. These minerals are denser than the adjacent gangue minerals to be carried by river downstream. These gold-bearing minerals are products of rock weathering that occurred on mountainous areas. These weathered gold-bearing minerals are transported downslope until such time, the gold is liberated and is deposited onto the river streams. Identified small-scale mining activities in the area are classified both as artisanal (e.g. incorporated with amalgamation) and gold-rush techniques (Maglambayan et al., 2005). Benguet, particularly the Acupan District, was known to produce 800 tons of gold ore in 1990 (Cooke, 1990). In addition, there were also trace elements and gold concentrates that were reported from Dalicno small-scale mines in Mankayan (Maglambayan, et al., 2005).

## 1.3 Significance of the study

1. The study can be used to perform an effective water quality monitoring in placer regions with active anthropogenic activities.
2. The study provides technical guidelines on detecting potential sites of population migration due to presence of gold-bearing mineral deposits.

## 1.4 Hypothesis

- Remote sensing geologic and water indices are useful in generating an effective environmental monitoring plan in placer regions

## 1.5 Research Objectives

To investigate the applicability of remote sensing in environmental monitoring, the following objectives were formulated.

**Primary Objective**

- To identify the subsections of infrared spectrum, which are suitable in delineating placer deposits and iron-bearing minerals, and detect their spatial and temporal dynamics to determine appropriate environmental monitoring stations

**Secondary Objectives**

1. To investigate the extensibility of optical and thermal satellite imaging in identifying placer deposits and iron-bearing minerals; and
2. To determine environmental factors that can affect complete detection of placer deposits and iron-bearing minerals.

## 1.6 Scope and limitations

The study was conducted with the following scopes and limitations.

1. The study was restricted on detection of potential locations of placer deposits, which did not involve delineation of active anthropogenic activities such small-scale mining and quarrying.
2. The study was focused on the possible application of infrared region of electromagnetic spectrum on delineating inland waters from land formation such as placer deposit and iron-bearing minerals.
3. The study discussed the extensibility and limitation of the method with respect to environmental elements such as rainfall rate, temperature, geology and geomorphological property of case study area.

# 2. LITERATURE REVIEW

## 2.1 Remote sensing using optical satellite imaging

Remote sensing or simply called earth observation is the process of examining the earth's ground features such as land covers, coastal waters and urban structures through the spatial data acquired at a distance by a satellite sensor (Campbell & Wynne, 2011). At present, the method has been widely used in monitoring the environment, catchment hydrology, forest fires and geology (Isidro et al., 2017). The method has been given emphasis due to its capability to distinguish and investigate a particular land use of interest by exploiting seasonal changes, health assessment of vegetation cover, provision of geomorphological data, and spatial correlation of ground survey data (Khorram et al., 2012). In remote sensing, the medium is the electromagnetic spectrum. It is composed of several forms of light with distinct energy, frequency and wavelength. In remote sensing, these light forms are typically distinguished by their range of wavelength (**Table 2-1**). Those light forms with longer wavelengths are more useful in satellite remote sensing. Light forms with short wavelengths are easily absorbed by the atmosphere's molecular constituents thus there is a reduced amount of radiance of transmitted signal from a ground object back to the satellite sensor.

**Table 2-1.** Spectral regions of electromagnetic spectrum

| Spectral regions | Wavelength (μm) | |
|---|---|---|
| | Min | Max |
| Gamma ray | 0 | 0.00003 |
| X-ray | 0.00003 | 0.003 |
| Ultraviolet | 0.003 | 0.38 |
| Visible spectrum | 0.38 | 0.72 |
| Infrared | 0.72 | 1,000 |
| Microwave | 1,000 | 300,000 |
| Radiowave | > 300,000 | |

Adapted from *Introduction to Remote Sensing* (p.60-62), by W. Emery, A. Camps and M. Cassola, 2017, United States: Elsevier

Sensors on board of satellites use different forms of light in the electromagnetic spectrum in the form of spectral regions. Light energy is sourced from the sun in the form of irradiance. The amount of irradiance absorbed and reflected by ground objects is sent back to the sensor in separate spectral regions. These spectral regions are further divided into subsections and are called spectral bands. Each spectral band produces a satellite image that appears as set of grayscale pixels with values in unit less digital numbers (DNs). This digital numbers represent brightness intensity based on the signal forwarded back to the sensor. The amount of radiance of each spectral band is highly affected by two factors; the atmospheric interference due to atmospheric constituents, and relative affinity of ground object to different forms of light. Furthermore, these digital numbers can be converted into physical units such as radiance ($W \cdot sr \cdot m^{-2}$) and reflectance (unit) for multi-sensor comparison (Emery et al., 2017). On the other hand, different forms of visible light and infrared light are the focus of optical remote sensing whereas thermal infrared light is used for thermal analysis. To generate a multispectral image or a thematic map, remote sensing process performs layer stacking that is a composite of two to three spectral bands only. Several combinations of spectral bands result to multispectral images that have

different functions. These functions include visual emphasis to geological formation, vegetation and ice covers, bare soil and smoke.

### 2.1.1 Band ratios in satellite optical imaging

Remote sensing offers a technique that applies indices or band rationing. Indices determine the ratio of preferred combinations of spectral bands (in the form of DN ratios) to demonstrate spectral variations of selected image objects with distinctive responses to selected band ratios (Alasta, 2011; Dogan, 2012). Moreover, band ratios emphasize spectral contrast among image objects, and provide additional information, which is not available from any single spectral band (Trinh, 2016). They generate thematic maps, which still preserve environmental factors such as slope, seasonal features and irradiance intensity, but do not reflect effects of shadows (Alasta, 2011; Trinh, 2016). Known indices are used to detect vegetation, open waters, regional geology, forest fire and active volcanoes. For instance, the Modified Normalized Difference Water Index (MNDWI), can be used to extract earth surfaces dominated by water, and separate them from open and vegetated lands (McFeeters, 1996; Xu, 2008). However, the index can only be used for sensors capable of detecting shortwave infrared (SWIR) such as the Landsat 7 ETM and 8 OLI (Koutsias & Pleniou, 2015) (**Table 2-2**). Its overlying principle concentrates on the fact that water bodies highly absorb SWIR whereas other land covers such as soil surface, vegetated areas and built-ups highly reflect it.

Furthermore, geology indices are used to extract open lands on satellite images, and to determine the underlying regional geology (Segal, 1982). An excellent example of

geology index is the Ferrous Mineral Ratio (FMR). Similar with MNDWI, it uses the infrared region. Iron-bearing rocks have noticeable reflectance at near-infrared (NIR) and SWIR, and areas concentrated with ferrous minerals generate FMR index values greater than one. Whereas other land covers and water bodies generate index values of less than zero (Xu H. , 2006). The index was previously tested using Landsat TM and ETM+ sensors (Murthy & Mallick, 1984; Segal, 1982; Alasta, 2011).

**Table 2-2.** Landsat-8 and RapidEye satellite images used in the study with corresponding acquisition dates

| **Scene** | | **Sensor** | | | | | | |
|---|---|---|---|---|---|---|---|---|
| **Satellite** | **Acquisition** | **Classification** | **Spectral Bands** | **Designation** | **Wavelength** | | | **Spatial resolution** |
| | Date | | | | *μm* | | | *meters* |
| Principal satellite provider | | | | | | | | |
| **Landsat-8** | 7-Feb-14 | Visible | 1 | Coastal aerosol | 0.43 | - | 0.45 | 30 |
| | 14-May-14 | | 2 | Blue | 0.45 | - | 0.51 | 30 |
| | 1-Jul-14 | | 3 | Green | 0.53 | - | 0.59 | 30 |
| | 22-Nov-14 | | 4 | Red | 0.64 | | 0.67 | 30 |
| | 26-Feb-15 | Infrared | 5 | Near Infrared (NIR) | 0.85 | - | 0.88 | 30 |
| | 2-Jun-15 | | 6 | Shortwave infrared (SWIR) 1 | 1.57 | - | 1.65 | 30 |
| | 20-Jul-15 | | 7 | Shortwave infrared (SWIR) 2 | 2.11 | - | 2.29 | 30 |
| | 27-Dec-15 | | 8 | Panchromatic | 0.5 | - | 0.68 | 15 |
| | | | 9 | Cirrus | 1.36 | - | 1.38 | 30 |
| | | Thermal | 10 | Thermal infrared (TIRS) 1 | 10.6 | - | 11.19 | 30 |
| | | | 11 | Thermal infrared (TIRS) 2 | 11.5 | - | 12.51 | 30 |
| Supplementary satellite provider | | | | | | | | |
| **RapidEye** | 7-Feb-14 | Visible | 1 | Blue | 0.44 | - | 0.51 | 30 |
| | 27-Sep-14 | | 2 | Green | 0.52 | - | 0.59 | 30 |
| | | | 3 | Red | 0.63 | - | 0.69 | 30 |
| | | | 4 | Red Edge | 0.69 | - | 0.73 | 30 |
| | | Infrared | 5 | Near Infrared (NIR) | 0.76 | - | 0.85 | 30 |

Adapted from "The Spectral Response of the Landsat-8 Operational Land Imager", by J. Barsi et al., 2014, *Remote Sensing, 6,* (p.10242); "RapidEye Imagery Product Specifications", *Planet,* (p.6)

### 2.1.2 Acquisition of image objects' spectral signatures

The use of image digital numbers (DNs) as basis for temporal analysis is technically not advisable due to following reasons (Al-Fares, 2013). Firstly, satellite position at its orbit varies every time its sensor captures images of the same Earth feature. The orbit determines the platform's altitude from the ground and its inclination. The platform's position affects the amount of solar irradiance that is received by the sensor. Secondly, each sensor has a distinctive sensitivity to brightness. In a raw image, pixel brightness is represented by a particular range of DNs, which is sometimes not adequate to assign distinct values to properly separate pixels with minimum brightness difference. These variations are resolved by adjusting DNs into physical units using scaling factors, such as radiance (watt per steradian per square meter). On the other hand, in order to incorporate corrections based on solar angle, specific amount of solar irradiance for each spectral band, and earth-sun distance during acquisition of image, the radiance is further calibrated into top-of-atmosphere (ToA) reflectance (Campbell & Wynne, 2011).

The spectral signature of an image object represents reflectance values of an image pixel at each spectral band. Different Earth features such as land covers, water bodies, vegetation and urbanized areas have distinct spectral response to each spectral band. The spectral response variation determines their specific spectral signatures, which make them separable and distinguishable during spectral analysis.

### 2.1.3 Ground surface temperature

Ground surface temperature varies on different land covers. Typically, it is regulated by soil moisture and seasonal changes. In remote sensing, ground surface temperature is useful in mapping exposed soil surface or turbid water from vegetated areas and clear water. Moisture content has more remarkable impact on temperature increase in bare soil over vegetated areas. Remote sensing sensors provide information on ground surface temperature by utilizing the thermal infrared region of electromagnetic spectrum. The amount of radiance reflected by a ground object back to the sensor can be calibrated into temperature units. Surface temperature can be utilized to distinguish alluvial mines in water bodies. In addition, surface temperature is also associated with the application of geology and water indices to confirm the boundaries between clear water and placer materials. The amount of vegetation determines the amount of heat being absorbed by the soil itself (Ogashawara & Bastos, 2012). Several studies show that the lack of proper land use planning leads to unwanted deterioration of soil. Mining is known for stripping of top soil and clay minerals. However, the prolong exposure of open lands can cause excessive absorption of heat thus resulting to higher temperature. Surface ground temperature are now being observed by a number of sensors such as Landsat 8 TIR, ASTER and NOAA AVHRR. These sensors use thermal spectral bands, which produce pixel values that are convertible into temperature. Recently, the Landsat 8 TIR sensor has the highest spatial resolution of thermal bands. Landsat-8 TIR sensor has two thermal bands between the wavelengths 10.60 and 12.51 μm (Barsi et al., 2014).

### 2.1.4 Geomorphological analysis using a Digital Elevation Model (DEM)

Digital elevation model (DEM) is typically generated from radar (Radio detecting and ranging) images, but optical image and lidar are also applicable through remote sensing and photogrammetric methods (Makineci & Karabork, 2016). Radar sensors can penetrate through the ground regardless of cloud coverage, part of the day (day or night) and climate. Radar images produce crude and embossed colourless images, which provide various spatial details such as elevation, contour, slope and gradient. In addition, DEMs are useful in the study of topography, age of land forms, and catchment characteristics. One way of using DEM is the application of hypsometric curve. Hypsometric curve is defined as the difference between the minimum and maximum elevation of a drainage basin (Perez-Pena et al., 2009). It determines the possible age of a drainage basin based on the amount of materials that have been transported at lower elevation. Moreover, DEMs are used to provide information on surface topography. Based on the recent studies, the application of DEM has been effective in discovering active ground areas in agreement with the application of remote sensing indices and ground surface temperature. The hypsometric curve of a sub-drainage basin can describe the existing condition of its topography (Ohmori, 1993).

# 3. METHODOLOGY

## 3.1 Geomorphological property of sub-drainage basins

The geomorphological property of each sub-drainage basin of Benguet catchment was based on the hypsometric curves and averaged slopes derived for each sub-drainage basin. Initially, each sub-drainage basin was divided into ten equal elevations. The total surface area for each elevation was calculated and plotted against the corresponding elevation. The resulting plot produced two different shapes as shown in **Figure 3-1**. Plot 1 (convex curve) describes a young basin, which is dominated by diffusive processes such as rock movement due to unstable land surface, rain splash and soil creep (Fernandes, F et al., 1997). It is expected that it has steep slope, and water flows rapidly over this area. In contrast, plot 2 (S-shaped curve) presents an old basin with which, dominated by fluvial processes and most of the rocks from high elevation were already transported at the bottom (Ohmori, 1993; Cohen et al., 2008). Furthermore, the geometry of each sub-basin was determined. Minimum, maximum, mean and standard deviation of slope were calculated.

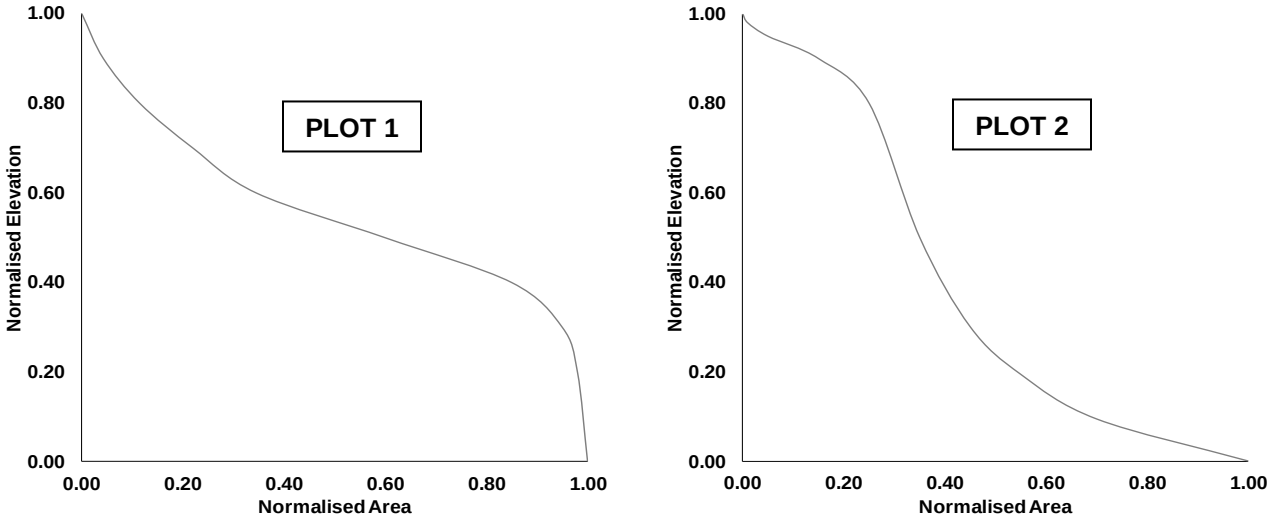


**Figure 3-1.** Principal forms of hypsometric curve
(a) Undeveloped sub-drainage basin; (b) Established sub-drainage basin

## 3.2 Acquisition of water quality data

Between the years 2014 and 2015, the water quality data collected by Miners Project B through the Environmental Management Bureau, CAR Region were used as baseline information on locating potential sites of placer deposits. These water quality data were secured in nine monitoring stations. In addition, the available water quality data that were selected included total suspended solids (TSS) and Hg concentrations, and their respective values were averaged quarterly. However, only the monitoring stations with working areas (e.g. river width) detectable within the 30 m by 30 m spatial resolution of Landsat-8 images (e.g. Agno-1, Agno-3, Agno-4, Agno-6) were nominated for spectral analysis to exclude pixels of aggregate land covers.

The acquired data from spectral analysis were utilized to understand the spatial variation in placer deposits as well as their temporal change quarterly. The plots of water quality data (e.g. TSS, Hg concentrations) against monitoring stations for each quarter were associated with the geomorphological properties of the sub-drainage basin with which, they were situated. Furthermore, other environmental elements were investigated in relation with the respective TSS and Hg concentrations at each monitoring station, and their potential influence on anthropogenic activities.

## 3.3 Detection of placer deposits and iron-bearing minerals using selected water and geology indices

Initially, the river networks and lakes of Benguet catchment that comprise of placer materials were identified using hydrological analyst function of a GIS software. Afterwards, the widths and extends of identified networks of rivers and lakes surrounding the placer regions were manually delineated based on a satellite image. Within the case study area, the land component (e.g. placer materials) was separated from inland waters (e.g. rivers and lakes) through the application of the Modified Normalized Difference Water Index (MNDWI) (McFeeters, 1996). In **Eqn. 1**, shortwave infrared-1 (SWIR-1) and green spectral bands of Landsat-8 OLI sensor were utilized in the algorithm, which was applied to eight images acquired for each quarter between the years 2014 and 2015. In this equation, the green band was used arbitrarily as both water bodies and land surface have insignificant responses (e.g. reflectance and absorbance) to it when compared with their responses to infrared band (Xu H. , 2006).

$$\text{MNDWI} = \frac{\text{Green} - \text{SWIR}}{\text{Green} + \text{SWIR}} \quad \textbf{(1)}$$

where Green = Green spectral band between 0.5-0.6 µm; SWIR = Shortwave Infrared spectral band between 1.55-1.75 µm

Afterwards, selected sections of infrared region were used to delineate sections of placer deposits with iron-bearing minerals. The Ferrous Mineral Ratio (FMR) index has been known to determine the level of iron concentration of a selected pixel based on the resulting ratio of shortwave infrared and near infrared bands (Alasta, 2011; Dogan, 2012; Trinh, 2016). The equation was applied to Landsat-8 spectral bands that corresponded to these spectral regions to delineate sections of placer deposit with iron-bearing minerals. In this case, the shortwave infrared band of Landsat-8 between 1.55 µm and 1.75 µm was nominated.

$$\text{FMR} = \frac{\text{SWIR}}{\text{NIR}} \quad \textbf{(2)}$$

where NIR = Near Infrared spectral band between 0.76-0.90 µm; SWIR = Shortwave Infrared spectral band between 1.55-1.75 µm

## 3.4 Detection of spectral signatures using optical imagery

### 3.4.1 Image calibration

The derivation of ToA reflectance using Landsat-8 OLI sensor images requires calibration of DNs using linear regression that employs rescaling factors (**Eqn. 3**). Each band has specific multiplicative ($M_p$) and additive ($A_p$) rescaling factors provided from image metadata. However, solar angle at nadir varies for every pixel within the image's

coverage (da Silva et al., 2016). A scene centre solar angle or sun elevation is applied after derivation of ToA reflectance (**Eqn. 4**). For this task, spectral bands 2 to 7 of Landsat-8 were selected. Afterwards, a 30 by 30 m pixel for each nominated monitoring station were selected. Each pixel was carefully evaluated if within the top-width of river stream. Those sections that were completely represented by pure pixel of placer deposit were considered for spectral analysis. Furthermore, the consistency of spectral signature of placer deposit was evaluated and tested in each quarter of years 2014 and 2015.

$$p\lambda' = M_p DN + A_p \quad \textbf{(3)}$$

where $p\lambda'$ = ToA planetary reflectance; $M_p$ = Multiplicative rescaling factor; DN = Standard product pixel values (Digital Numbers); $A_p$ = Additive rescaling factor

$$p\lambda = \frac{p\lambda'}{\cos(\theta_{SZ})} = \frac{p\lambda'}{\sin(\theta_{SE})} \quad \textbf{(4)}$$
$$\theta_{SZ} = 90^o - \theta_{SE}$$

where $p\lambda$ = ToA reflectance with corrected solar angle; $\theta_{SZ}$ = Zenith angle; $\theta_{SE}$ = Sun elevation

For the case study, **Table 3-1** below presented the values of rescaling factors and sun elevation angles that were used in **Eqns. 3** and **4** for each image scene in years 2014 and 2015. The calibrated pixels' digital numbers to ToA reflectance, were expressed within the range of zero to one.

**Table 3-1.** Rescaling factors for the Landsat-8 images in 2014 and 2015

| **Bands** | **Rescaling factors** | | **Sun Elevation** | | | | | | | |
|---|---|---|---|---|---|---|---|---|---|---|
| | | | **2014** | | | | **2015** | | | |
| 2-7 | $Mult_{ref}$ | $Add_{ref}$ | $1^{ST}$ | $2^{ND}$ | $3^{RD}$ | $4^{TH}$ | $1^{ST}$ | $2^{ND}$ | $3^{RD}$ | $4^{TH}$ |
| | 0.00002 | -0.1 | 48 | 67 | 65 | 49 | 53 | 66 | 65 | 44 |

### 3.4.2 Atmospheric correction of spectral bands

A simple dark object subtraction (DOS) was used to remove atmospheric residuals of Landsat-8 images (Gilmore et al., 2015). Atmospheric residuals increase the reflectance received by the satellite sensor due to atmospheric constituents (e.g. atmospheric gases). In this method, it was assumed that there is an object in the image at minimum reflectance such as dark lake bottom, which is the result of atmospheric scattering (Chavez Jr., 1988). The minimum reflectance value was detected through the image histogram of the case study area. Afterwards, the minimum pixel reflectance of each spectral band was deducted to all the pixels.

## 3.5 Temperature derivation using Landsat-8 thermal images

Moreover, bands 10 and 11 of Landsat-8 TIRS sensor was selected and calibrated into radiance or brightness temperature using **Eqn. 5**. It was followed by calibration into temperature using **Eqn. 6**. The values of $K_1$ and $K_2$ constants in **Eqn. 6** are also listed in the image metadata (**Table 3-2**) (Kamran et al., 2015).

$$L_\lambda = M_L DN + A_L \quad \textbf{(5)}$$

where $L_\lambda$ = Radiance; $M_L$ = Multiplicative rescaling factor; DN = Standard product pixel values (Digital Numbers); $A_T$ = Additive rescaling factor

$$T = \frac{K_2}{\ln(\frac{K_1}{L_\lambda} + 1)} - 273.15 \quad \textbf{(6)}$$

where $L_\lambda$ = Radiance; $K_1$ = Band-specific thermal conversion constant 1; $K_2$ = Band-specific thermal conversion constant 2

**Table 3-2.** Rescaling factors for the Landsat-8 thermal band

| Band | $Mult_{ref}$ | $Add_{ref}$ | $K_1$ | $K_2$ |
|---|---|---|---|---|
| 10 | 0.10 | 0.0003342 | 775 | 1321 |

The detected temperatures at sensor were atmospherically corrected through the algorithm offered by PCI Geomatics software. In contrast, a relationship between MNDWI and ground surface temperature was derived using a linear regression model using **Eqn. 7**.

$$I_{MNDWI} = MT + Y \quad \textbf{(7)}$$

where T = Surface temperature; $I_{MNDWI}$ = Modified Normalized Difference Water Index

## 3.6 Flowsheet of spatial data process

For absolute values such as reflectance used to define spectral signature as well as the thematic map of ground surface temperature, atmospheric corrections were applied. In contrast, the use of band ratios such as FMR and MNDWI indices did not need this sort of pre-processing level since they only emphasize distinct responses of image objects to selected spectral bands, which do not involve absolute values (**Figure 3-2**). Afterwards, Landsat-8 bands 2 to 7 were utilized to generate thematic maps of MNDWI and FMR indices whereas Landsat-8 bands 10 and 11 were used to generate thematic maps of land surface temperatures in each quarter of years 2014 and 2015. In contrast, Rapid Eye high spatial resolution (5 m) images were used as visual basis on the possible changes in spectral signatures of pixels over placer deposits in each quarter.

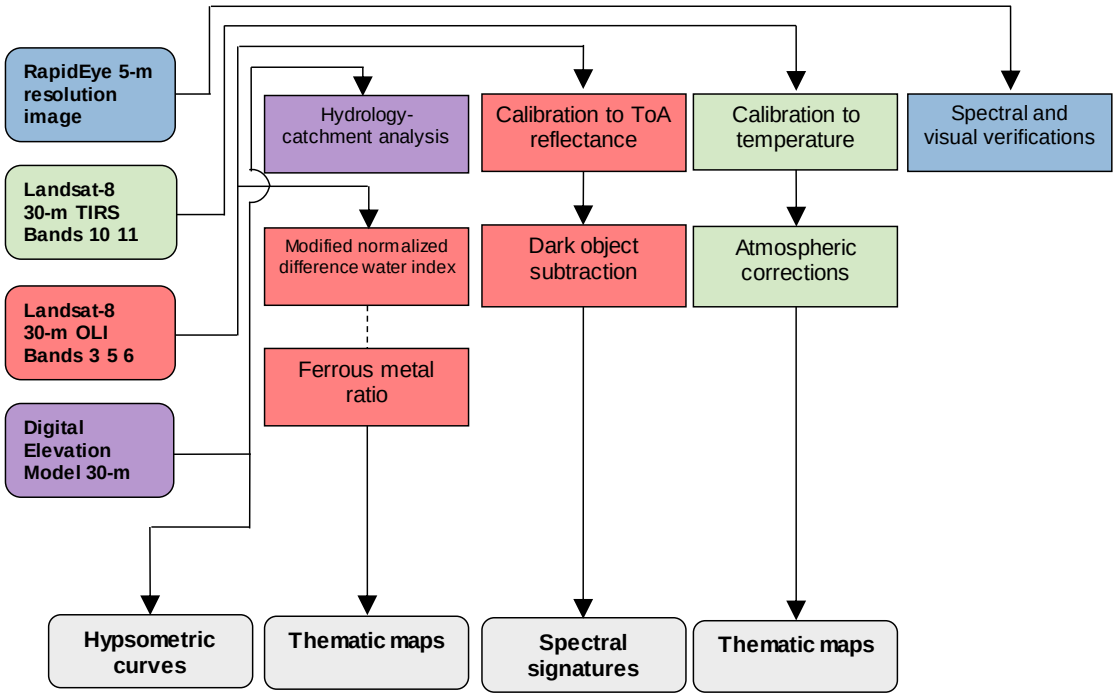


**Figure 3-2.** Flowsheet of satellite images pre-processing

# 4. RESULTS AND DISCUSSION

## 4.1 Observed TSS and Hg concentration levels in years 2014 and 2015

The observed concentration levels of TSS and mercury (Hg) were summarized in graphs on **Figure 4-1**. Based on **Figure 4-1A**, Agno-2 monitoring station located north of Binga Lake had observable TSS concentration level throughout the years 2014 and 2015. The TSS concentration levels were at decreasing rate starting from first quarter to third quarter. During the initial quarter of 2015, its TSS concentration level reached 2,994 $mgL^{-1}$, which was recorded as the second highest within the two years. Alternatively, Agno-3 monitoring station located on a tributary south of Ambuklao Lake resulted to 5,800 $mgL^{-1}$ during the second quarter of 2014. It was recorded as the highest TSS concentration level within the two years. Afterwards, high TSS concentration level was still observed over Agno-3 during the initial quarter of 2015 at 487 $mgL^{-1}$.

In contrast, high Hg concentration levels were consistently observed over Agno-2 monitoring station with the highest recorded value of 14 $\mu gL^{-1}$ during the initial quarter of 2014 (**Figure 4-1C**). In year 2015, it was the only monitoring station where Hg concentration was detected. Observable Hg concentrations were recorded over Agno-2 during the first, second and fourth quarters as shown in **Figure 4-1D**. On the other hand, the rest of the monitoring stations were examined to have moderate Hg concentration levels between 7.4 and 8.4 $\mu gL^{-1}$ during the second quarter of year 2014 only (**Figure 4-1C**). Overall, observed TSS and Hg concentration levels were recorded lowest during wet season (e.g. third quarter). During dry season, most of the monitoring stations exceeded

the acceptable mercury concentration level from 4 $\mu gL^{-1}$ to 8 $\mu gL^{-1}$ and TSS from 100 $mgL^{-1}$ to 150 $mgL^{-1}$ for both Class C and D rivers.

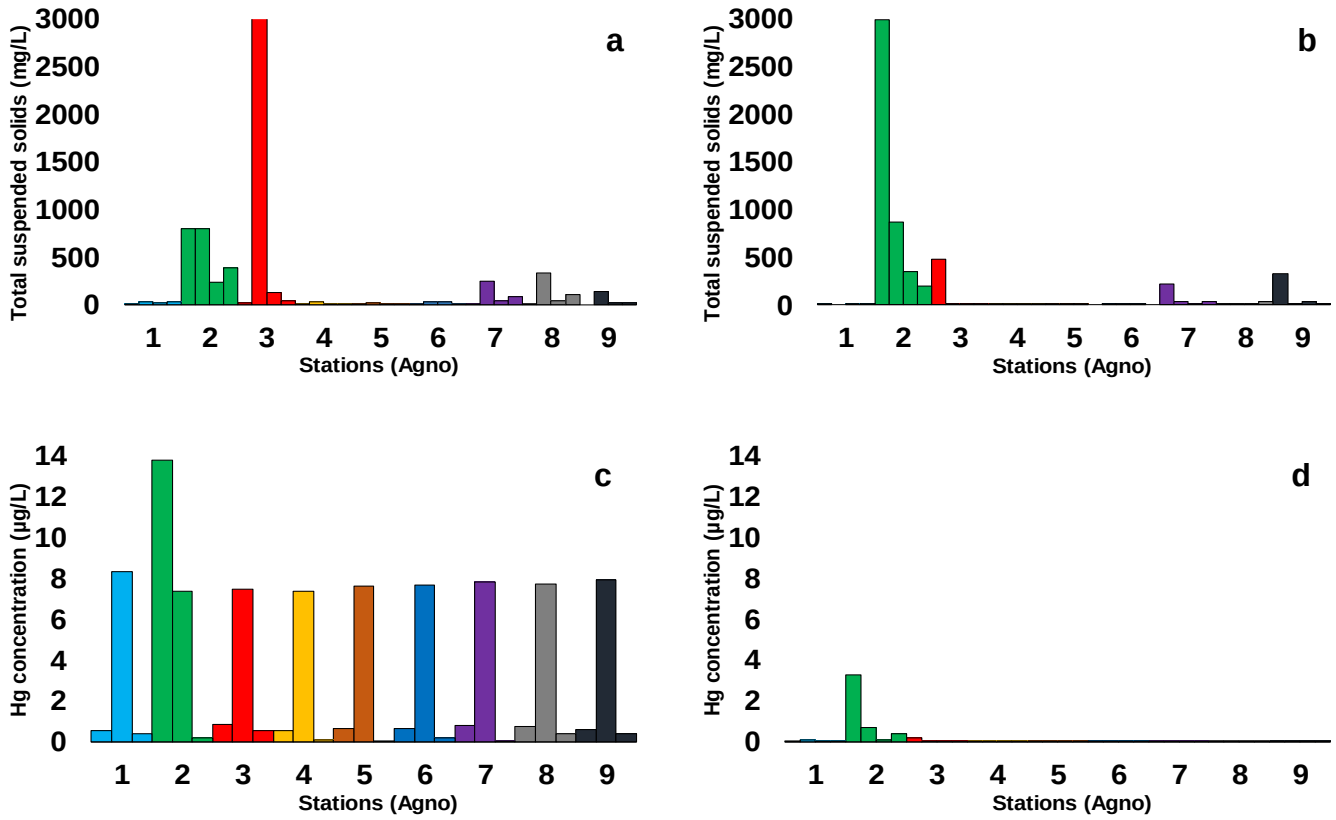


**Figure 4-1.** Summary of TSS and Hg concentration levels at each monitoring station (Agno-1 to 9) (a) 2014 $1^{ST}$-$4^{TH}$ Quarters TSS; (b) 2015 $1^{ST}$-$4^{TH}$ Quarters TSS; (c) 2014 $1^{ST}$-$3^{RD}$ Quarters Hg concentration; (d) 2015 $1^{ST}$-$3^{RD}$ Quarters Hg concentration

## 4.2 Geomorphological analysis

Among the monitoring stations in **Figure 4-1**, river sections with top-width within the 30 m by 30 m spatial resolution of Landsat-8 were selected for spatial and temporal analyses (e.g. geomorphology, index application). The river sections that enclosed the monitoring stations Agno-2, Agno-3, Agno-4 and Agno-6 were within this criterion as presented in **Figure 4-2**.

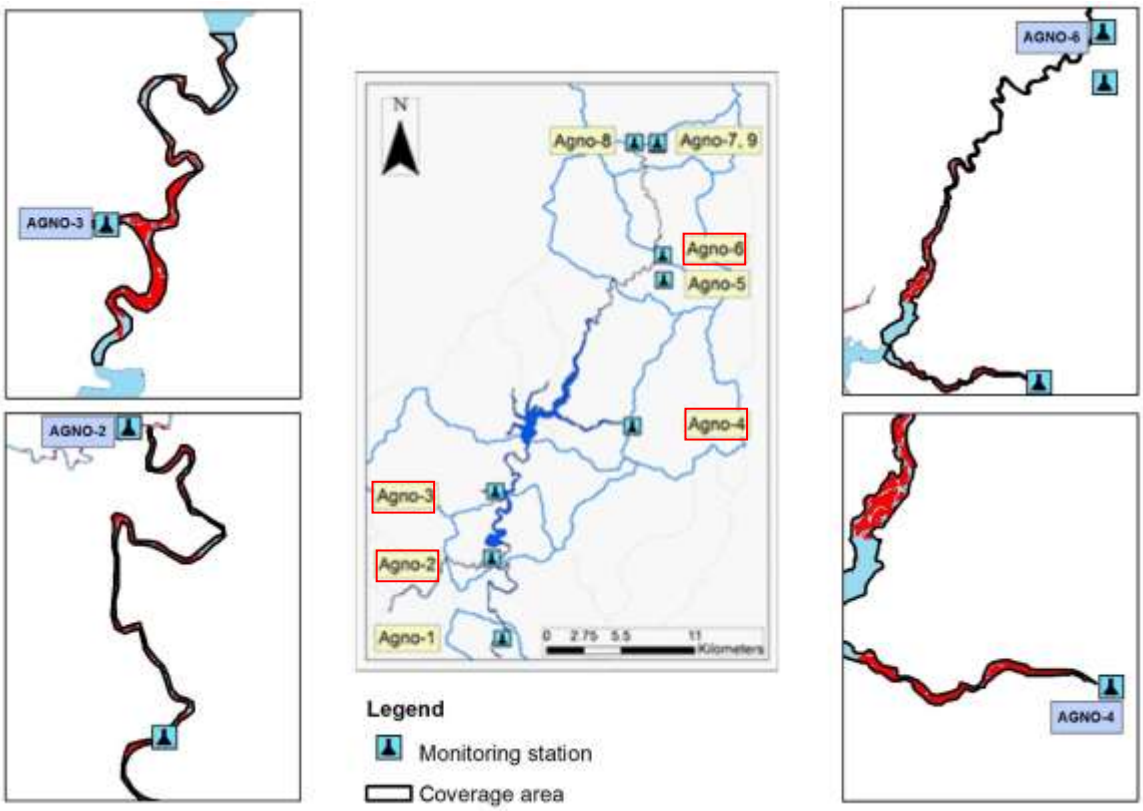


**Figure 4-2.** Selected monitoring stations and their corresponding area coverages
(a) Agno-2; (b) Agno-3; (c) Agno-4; (d) Agno-6

Upon the application of hypsometric analysis, the selected river sections that comprised Agno-3 and Agno-4 monitoring stations produced convex hypsometric curves (**Figure 4-3A**). These hypsometric curves did not necessarily reveal undeveloped age of sub-drainage basins that encompassed Agno-3 and Agno-4 monitoring stations. Rather, they conveyed the possible active ground movements over their surrounding mountains due to diffusive processes found on mountain slopes (**Figure 4-3A**). These monitoring stations were situated on small river tributaries that were least affected by strong waterflow from the upstream. On the other hand, the active ground movement (e.g. diffusive processes) could lead to exposure of iron-bearing minerals, which are susceptible to weathering. Among these sub-drainage basins, Agno-3 had consistent

noticeable TSS concentration levels during the first quarter of years 2014 and 2015. Whereas high Hg concentration level was detected for both Agno-3 and Agno-4 during the second quarter of 2014 (**Figure 4-1A-C**). These TSS and Hg concentration levels were presumed to be product of small-scale gold mining. In Benguet catchment, suspended solids are naturally generated due to high rainfall rate, which is experienced during the third quarter of the year only. Observable TSS concentration levels during dry season (e.g. first and second quarter), and generation of mercury could be the product of anthropogenic activities.

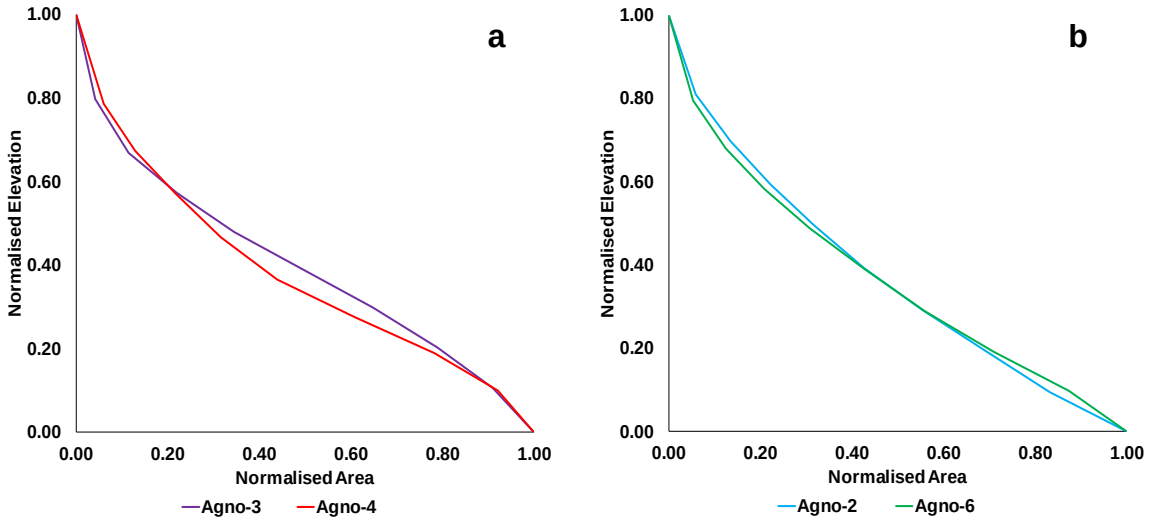


**Figure 4-3.** Potential age of each sub-basin containing the monitoring stations
(a) Monitoring stations over young sub-drainage basin; (b) Monitoring stations over old sub-drainage basin

In contrast, Agno-2 Agno-6 were determined as established sub-drainage basins as they generated concave curves (**Figure 4-3B**). Unlike the Agno-3 and Agno-4 monitoring stations, they were situated over the primary river network. This river section received strong waterflow from the upstream, which continuously washed-out placer materials and produced established topography. These sub-drainage basins were highly associated with

fluvial processes found in river networks. However, the Agno-2 monitoring station was observed to consistently produced high TSS level during the first quarter of years 2014 and 2015 and decreasing until the third quarter of these years. Similarly, Hg concentration as high as 3.79 $\mu gL^{-1}$ was observed during the first and second quarters of years 2014 and 2015. In contrast, Agno-6 monitoring station produced noticeable Hg concentration level during the second quarter of year 2014 only (**Figure 4-1C**). Despite the minimal ground movement over these sub-drainage basins, this section of the river network still rested over the quartz diorite intrusive, which continuously exposed placer materials and replenished them by fluvial processes.

Furthermore, Agno-6 had the highest mean slope among the four monitoring stations at 27.39 degrees as shown in **Table 4-1**. Similarly, it had the highest standard deviation of 10 degrees, which signified high variation of hill slope within its sub-drainage basin. Whereas Agno-2, Agno-3, Agno-4 had lower mean slope between 25 and 26 degrees. To conclude, the slope variation in each sub-drainage basin did not influence the generation rate of placer materials as well as the scale of its anthropogenic activities.

**Table 4-1.** Slope details of selected sub-drainage basin

| **Stations** | **Min** | **Max** | **Mean** | **Standard deviation** |
|---|---|---|---|---|
| | *Degrees* | | | |
| Agno-2 | 0.33 | 60.55 | 25.16 | 9.32 |
| Agno-3 | 0.33 | 67.33 | 25.56 | 9.36 |
| Agno-4 | 0.33 | 65.61 | 26.86 | 9.71 |
| Agno-6 | 0.47 | 68.11 | 27.39 | 9.99 |

## 4.3 Application of Modified Normalized Difference Water Index (MNDWI)

The application of MNDWI over the Landsat-8 images generated complete separation between Benguet River and potential locations of placer deposit. After the index was applied, the river entirely covered by clear water had absorbed the SWIR light, and it produced MNDWI values greater than zero as high as 0.50 in the generated thematic map (**Figure 4-6A-B**). In contrast, placer deposits had reflected SWIR more than the green light, and they produced negative MNDWI values as low as -0.35. Between the first and second quarters of 2014 and 2015, there was a minimal increase in surface coverage of placer deposit within the scope of selected monitoring stations (Agno-1, Agno-3, Agno-4 and Agno-6) (**Figure 4-4**).

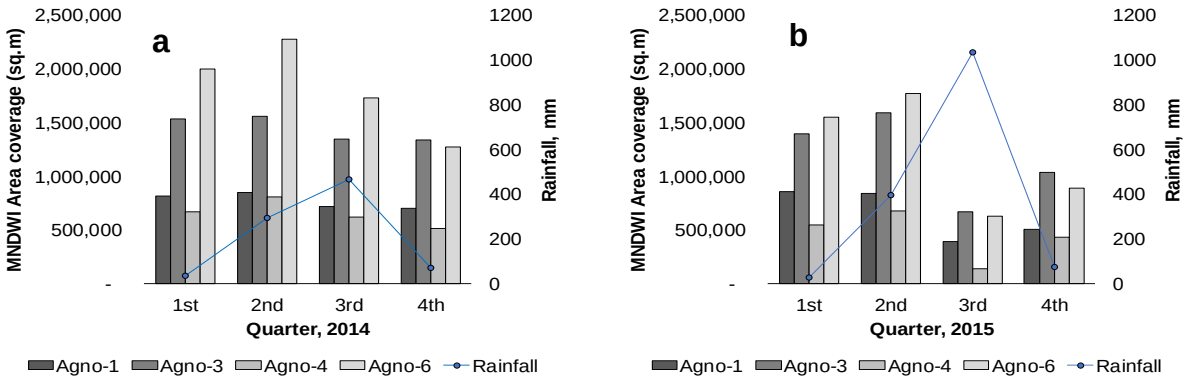


**Figure 4-4.** Change in surface area coverage of detected placer deposit using Modified Normalized Difference Water Index (MNDWI)
(a) Placer materials area coverage in 2014; (b) Placer materials area coverage in 2015

Furthermore, rainfall rate during the second quarter within the two years was higher compared with the first quarter by an average of 316 mm. During the quarter, there was a possible transfer of rock materials from high to low elevation, which was instigated by moderate rainfall. During the third quarter, rainfall rate increased as high as 1,000 mm.

The heavy rainfall led to river overflow, which covered selected sections of placer deposit whereas its sections located near the river discharge outlet were extensively washed-out. In **Figure 4-5**, clear deep water was represented in dark blue colour whereas light blue colour represented mixture of water and placer materials producing mudflow as shown during the third quarter of year 2015 for both Ambuklao and Binga lakes. This phenomenon led to noticeable decrease in area coverage of placer deposit (**Figure 4-4**). During the fourth quarter, rainfall rate decreased by an average of 70 mm. In 2014, there was a slight decrease in area coverage from third to fourth quarter whereas a minimal increase was observed in 2015.

In **Figure 4-6A-B**, thematic maps were generated for each quarter of years 2014 and 2015 to present the delineation between inland waters and placer deposit. Clear water (e.g. Positive MNDWI values) was presented in blue colour whereas various placer materials (e.g. negative MNDWI values) were displayed in green, yellow and red colours.

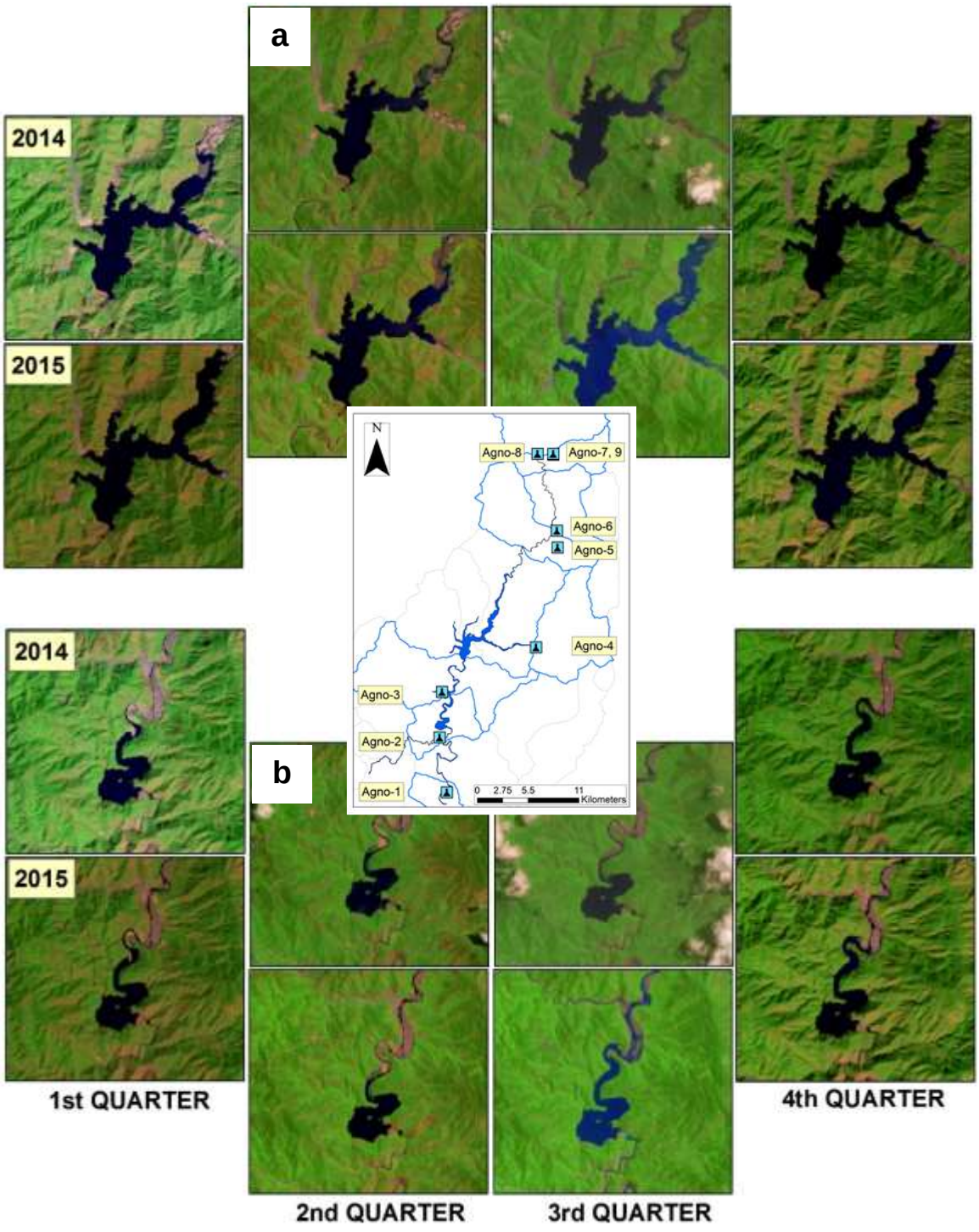


**Figure 4-5.** Changes in main river streams in each quarter
(a) Near Ambuklao Lake; (b) Near Binga Lake
Note: Application of Landsat-8 OLI sensor's spectral bands 6,4,2 (SWIR, red, blue bands)

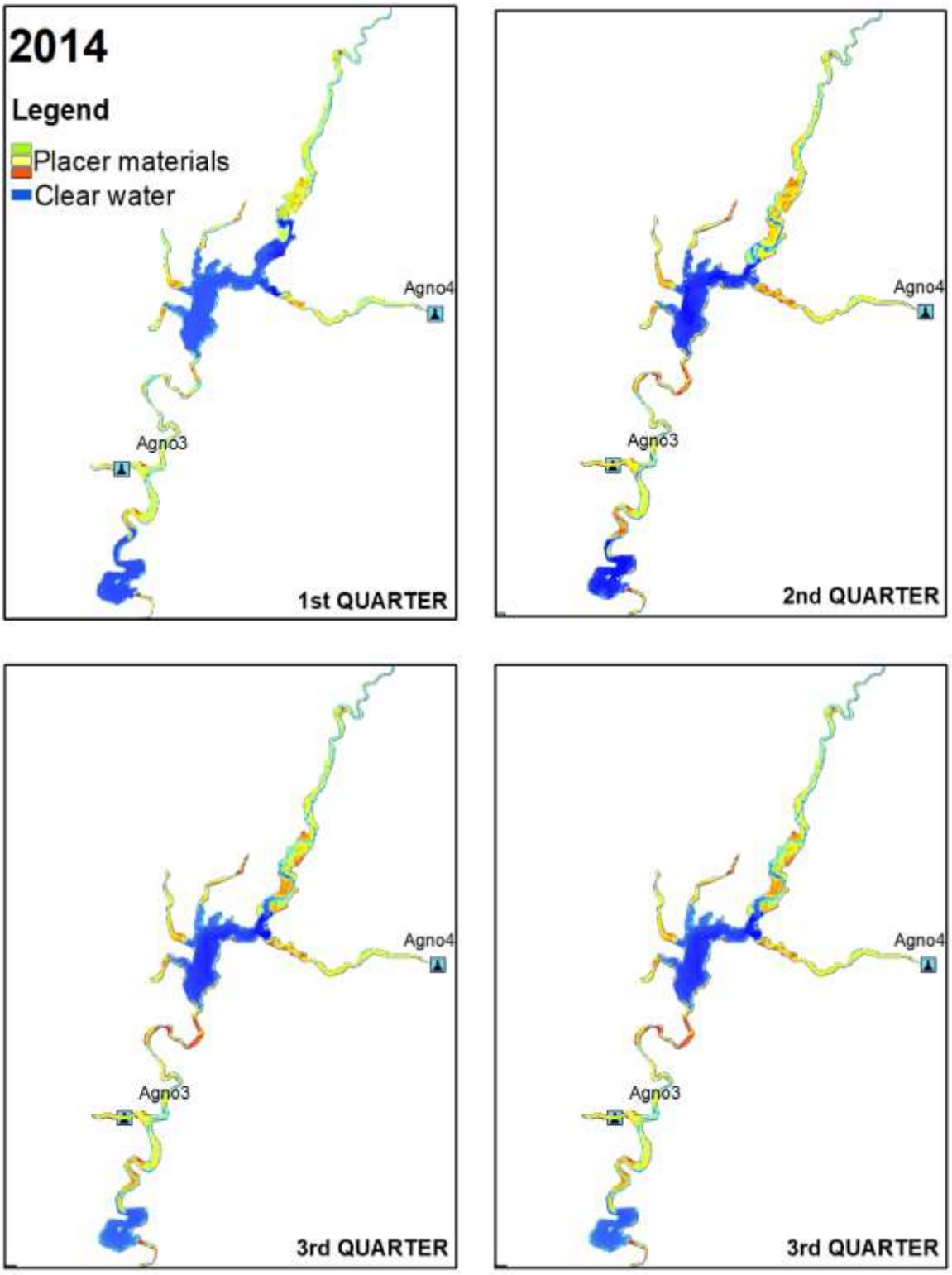


**Figure 4-6A.** Delineation of clear water and placer mines using Modified Normalized Difference Water Index (MNDWI) in 2014

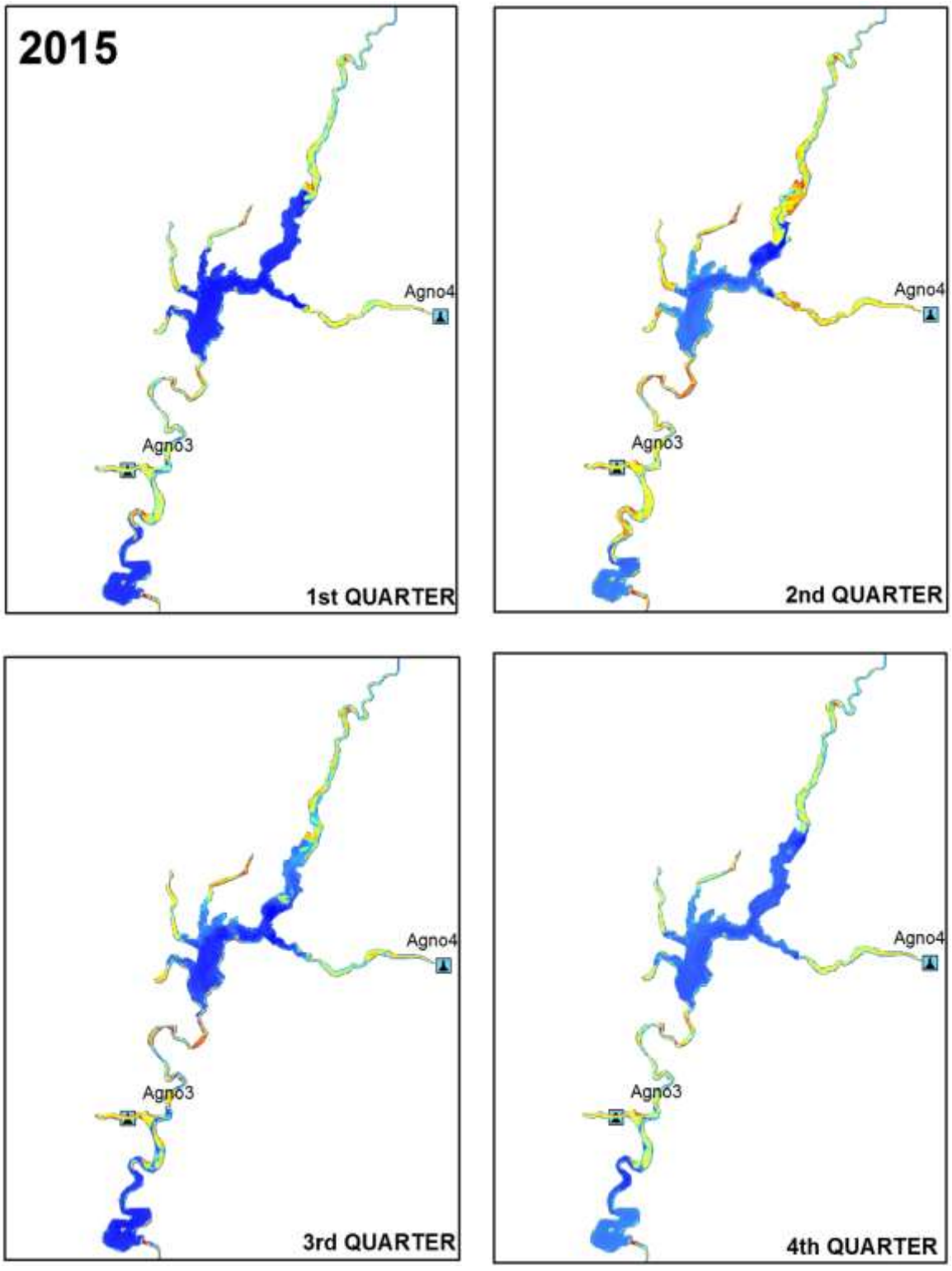


**Figure 4-6B.** Delineation of clear water and placer mines using Modified Normalized Difference Water Index (MNDWI) in 2015

## 4.4 Application of Ferrous Mineral Ratio (FMR)

Upon the application of FMR index, iron-bearing minerals within the placer regions were delineated. The iron-bearing minerals produced FMR index value of 1 whereas other placer materials and water bodies had null FMR index value. The minimal range of FMR index value over the iron-bearing minerals was affected by the continuous replenishment of these placer materials thus exposing only the minerals with low iron content. Furthermore, only small section of placer deposits was found to contain iron-bearing minerals. The acquired area coverages for the selected monitoring stations were smaller compared with those acquired for placer deposits using MNDWI. Therefore, only selected sections of placer deposit were potential for small-scale gold mining. During the third quarter of years 2014 and 2015, iron-bearing minerals were almost not detectable. The SWIR and NIR lights were absorbed by the overflowing water during heavy rains. In addition, the acquired area coverage of iron-bearing minerals was not comparable for each quarter as they were being replenished at irregular intervals as shown in **Figure 4-7**.

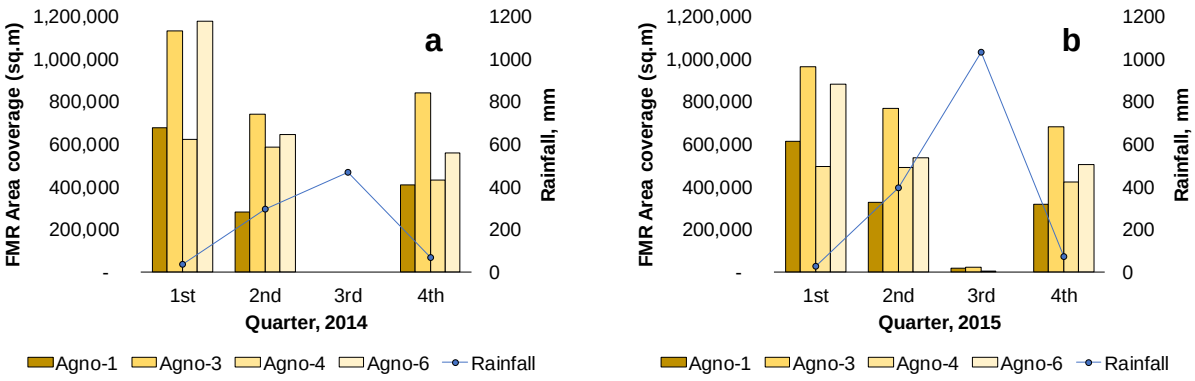


**Figure 4-7.** Change in surface area coverage of detected ferrous minerals using Ferrous Mineral Ratio

Meanwhile, FMR index can be utilized to identify portions of placer deposit that have traces of ferrous minerals. If gold in Benguet Region is highly associated with pyrite and chalcopyrite, which contain iron metals, the identified sites with iron-bearing minerals are potential for anthropogenic mining activities. Identification of these sites can assist to formulate an excellent regular water quality monitoring program. In **Table 4-2**, temporal variation in area coverage of both placer deposit and iron-bearing minerals within the entire Benguet catchment was summarized. The table presented that these indices could capture the full extent of placer deposit during the first and second quarters of the year when rainfall rate was minimal and ground movement was less evident.

**Table 4-2.** Summary of surface area coverage of placer deposit using MNDWI and detected ferrous minerals using FMR

| 2014 AREA COVERAGE ($km^2$) | | | | |
|---|---|---|---|---|
| **Quarter** | **1ST** | **2ND** | **3RD** | **4TH** |
| **Acquisition Date** | 2014.02.07 | 2014.05.14 | 2014.07.01 | 2014.11.22 |
| Placer deposits | 6.60 | 7.20 | 5.18 | 5.81 |
| Ferrous minerals | 4.36 | 2.73 | n.d. | 2.60 |

| 2015 AREA COVERAGE ($km^2$) | | | | |
|---|---|---|---|---|
| **Quarter** | **1ST** | **2ND** | **3RD** | **4TH** |
| **Acquisition Date** | 2015.02.26 | 2015.06.02 | 2015.07.20 | 2015.12.27 |
| Placer deposits | 5.81 | 6.50 | 2.77 | 4.07 |
| Ferrous minerals | 3.63 | 2.55 | n.d. | 2.29 |

This analysis presented that iron-bearing minerals reflected more infrared light compared with the remaining sections of placer deposit. It can be concluded that iron-bearing minerals reflect more infrared light than other land forms. On the other hand, clear waters highly absorbed near-infrared and shortwave infrared lights, which produced null values using the FMR ratio.

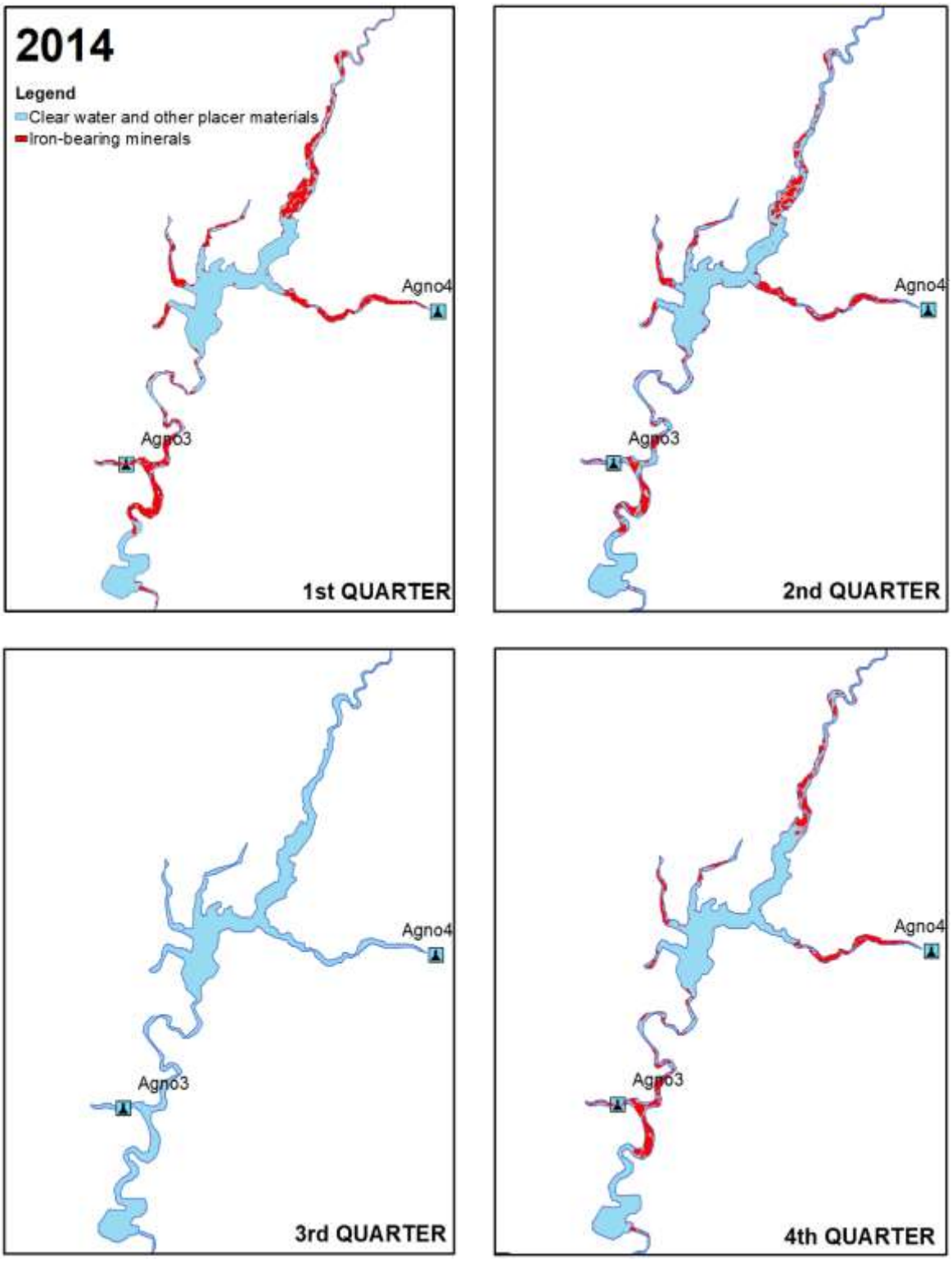


**Figure 4-8A.** Delineation of clear water and placer mines using Ferrous Minerals Ratio in 2014

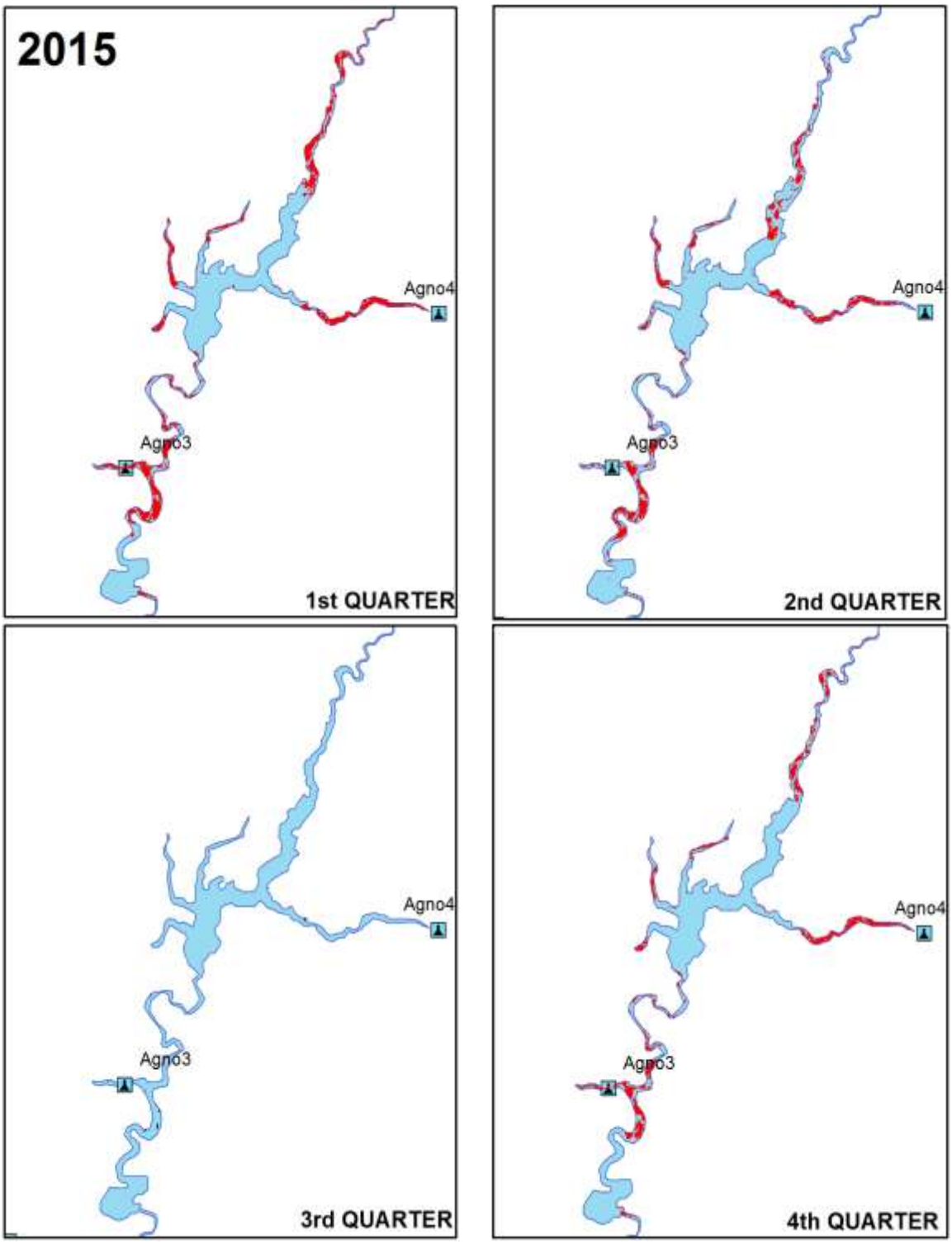


**Figure 4-8B.** Delineation of clear water and placer mines using Ferrous Minerals Ratio in 2015

## 4.5 Detected spectral signature of placer deposit

The spectral signature of placer deposits was presented in **Figure 4-9**. Placer deposit had low reflectance values in all spectral bands. Between the wavelength from 1 to 1.5 µm, there was a constant value and a decrease afterwards. Based on detected spectral signature of placer deposit, its spectral response to near-infrared and shortwave infrared was almost equal. During heavy rains, this spectral signature changed, and a reflectance increase at 1 µm was observed. This is the aggregate spectral signature of turbid water/ mudflow, which was observed flowing over selected sections of placer deposit during the second and third quarter of 2014 and 2015.

Furthermore, the spectral signature of iron-bearing minerals is slightly similar with placer deposit (**Figure 4-10**). However, in iron-bearing minerals, reflectance at SWIR is higher than at NIR region. This spectral signature is similar with plots from literature reviews for iron-bearing minerals. The increase of reflectance at SWIR was determined by the concentration level of iron. Any decrease in reflectance after 1 um was due to presence of water.

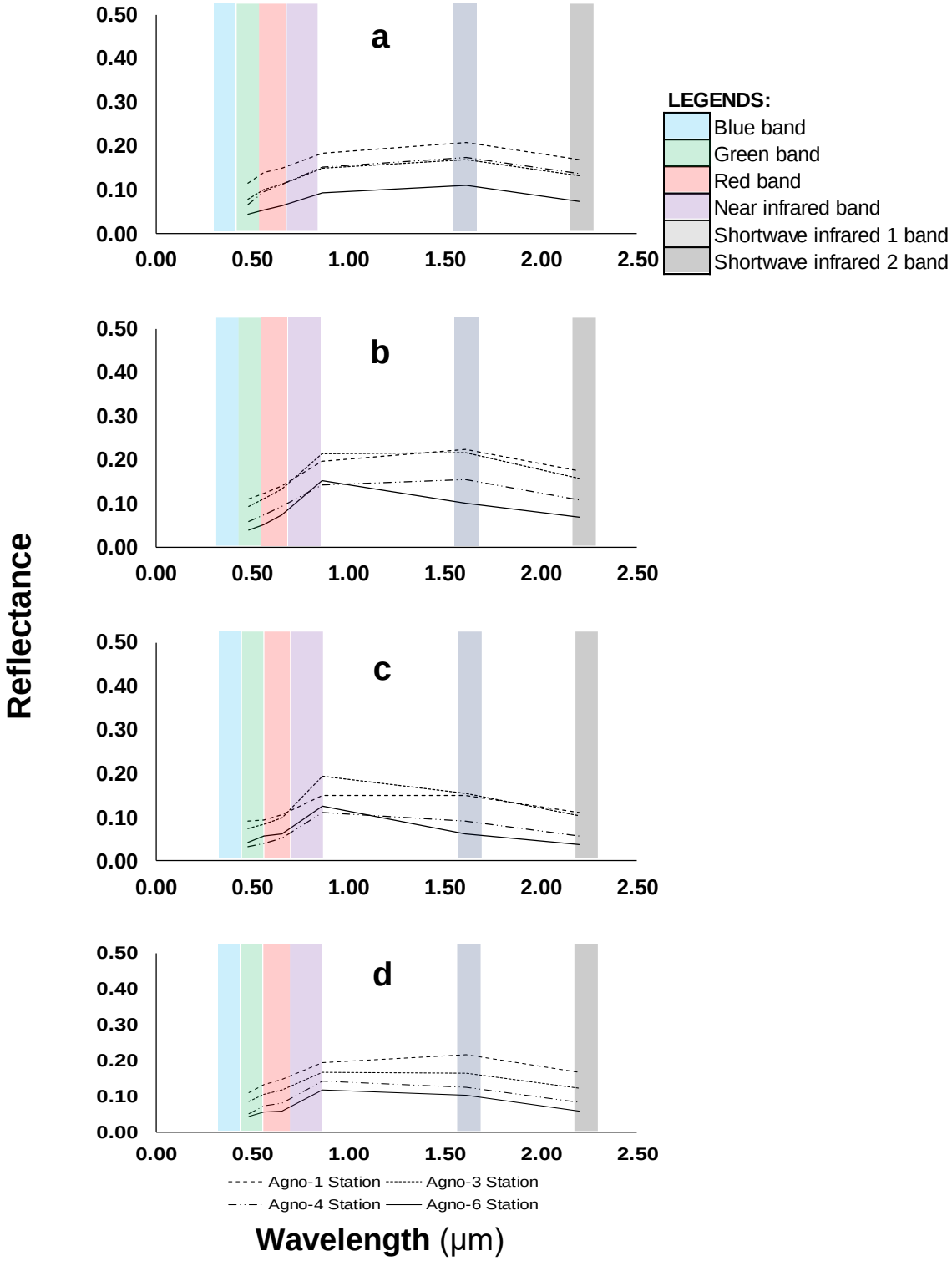


**Figure 4-9.** Detected spectral signatures over selected monitoring stations
(a) 1ST Quarter; (b) 2ND Quarter; (c) 3RD Quarter; (d) 4TH Quarter

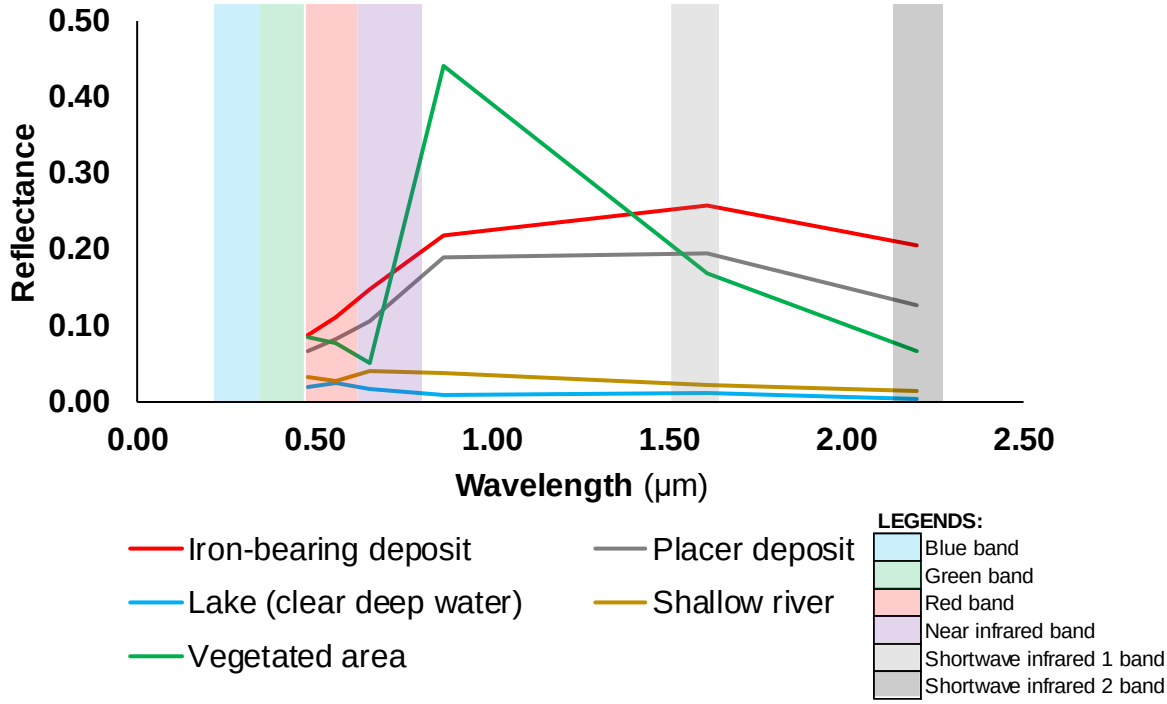


**Figure 4-10.** Difference in spectral signature between placer deposit and iron-bearing minerals

## 4.6 Surface temperature difference between placer deposit and river

The calibrated thermal image scenes illustrated temperature variance from 0 to $40^0$ C across the Benguet River (**Figure 4-11A-B**). During the initial quarters of 2014 and 2015, placer deposit absorbed more thermal infrared compared with inland waters. During the second quarter, selected river segments had temperature as high as $26^0$ C (green colour). This can be an indicator of water scarcity during the period, exposing portion of placer deposits at lower elevation. In contrast, temperature difference between placer deposit and river was not distinguishable during the third quarter. The third quarter of the year had recorded the highest rainfall rate for three months. The continuous rainfall led to mudflow covering placer deposits, which lowered its surface temperature, and made them

undetectable. During the last quarter of the year, temperature difference was only detectable between the river and placer deposits in wide areas.

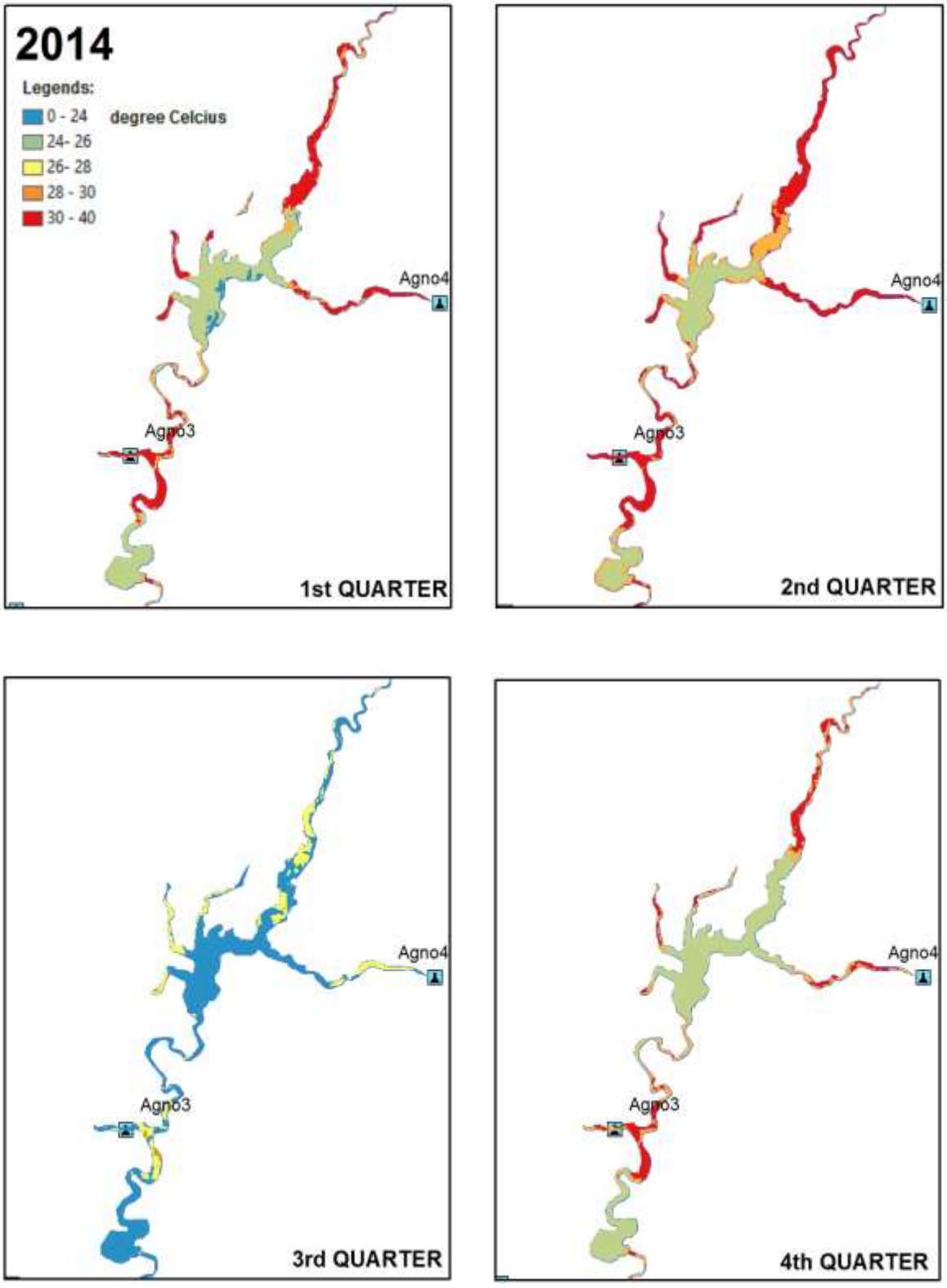


**Figure 4-11A.** Surface temperature of river and placer mines in 2014

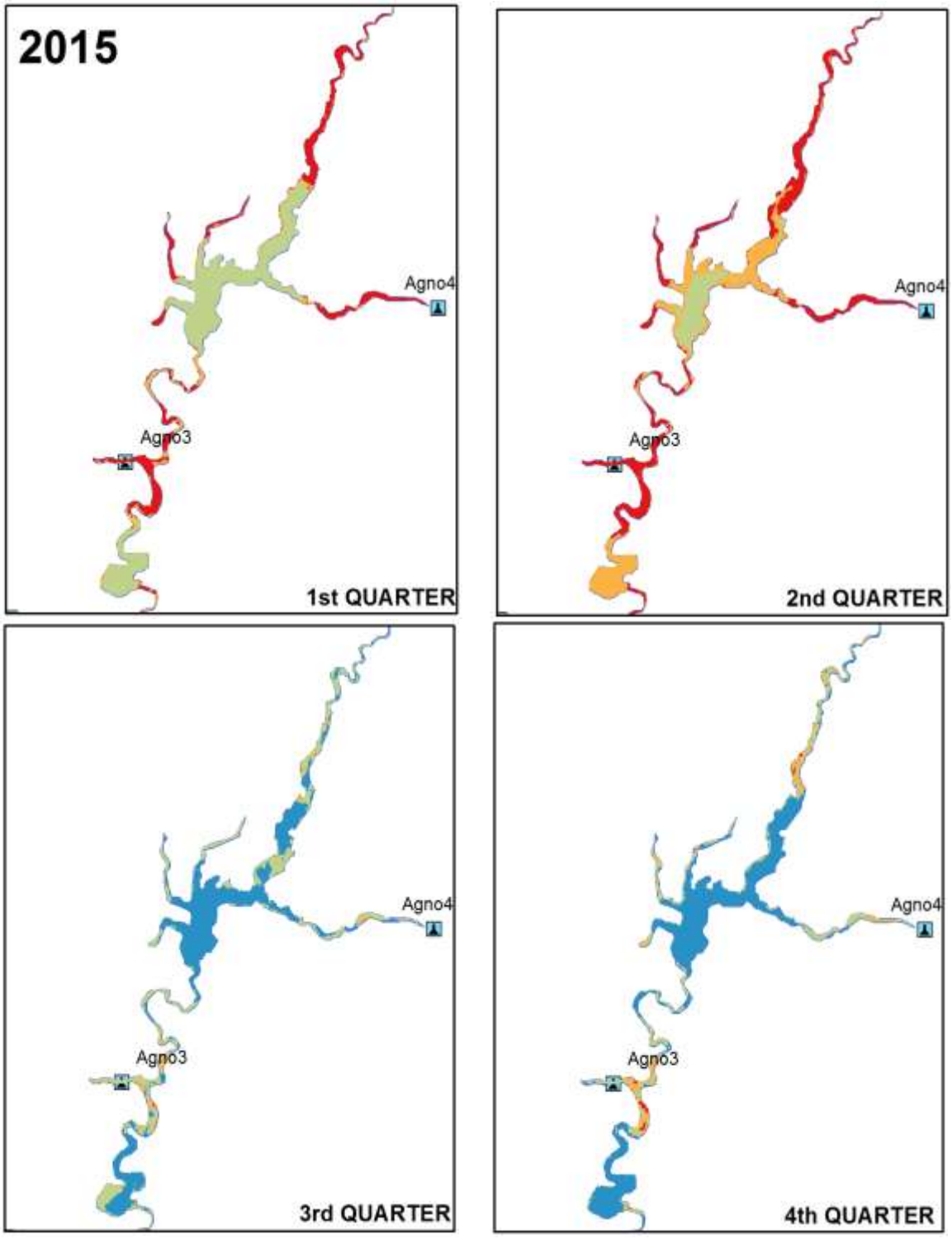


**Figure 4-11B.** Surface temperature of river and placer mines in 2015

## 4.7 Relationship between MNDW index and surface temperature

An inverse direct relationship between MNDWI values and surface temperature was generated using 50 random test points within the Benguet catchment. The generated inverse linear equation has a coefficient of determination ($R^2$) of 77% and a correlation coefficient of -0.88 (**Figure 4-12**). The high value of $R^2$ demonstrated the adequacy of the generated model to represent the variation in MNDWI values at all field condition. In contrast, the negative correlation presented the inverse relationship between MNDWI and surface temperature. Furthermore, the test points above the horizontal axis were those sampled over clear sections of inland waters whereas test points below the horizontal axis were from placer deposits. Based on this plot, placer deposits, with negative MNDWI values typically have surface temperature ranging from 30 to 45 degrees Celsius while inland waters temperature ranges from 20 to 30 degrees Celsius. The computed root-mean-square error (RMSE) for the model was 0.03 only, which is insignificant. Therefore, there was a very low disagreement between the observed and predicted values of MNDWI.

$$\mathrm{I_{MNDWI}} = -0.01(\mathrm{T}) + 0.33 \qquad \textbf{(8)}$$

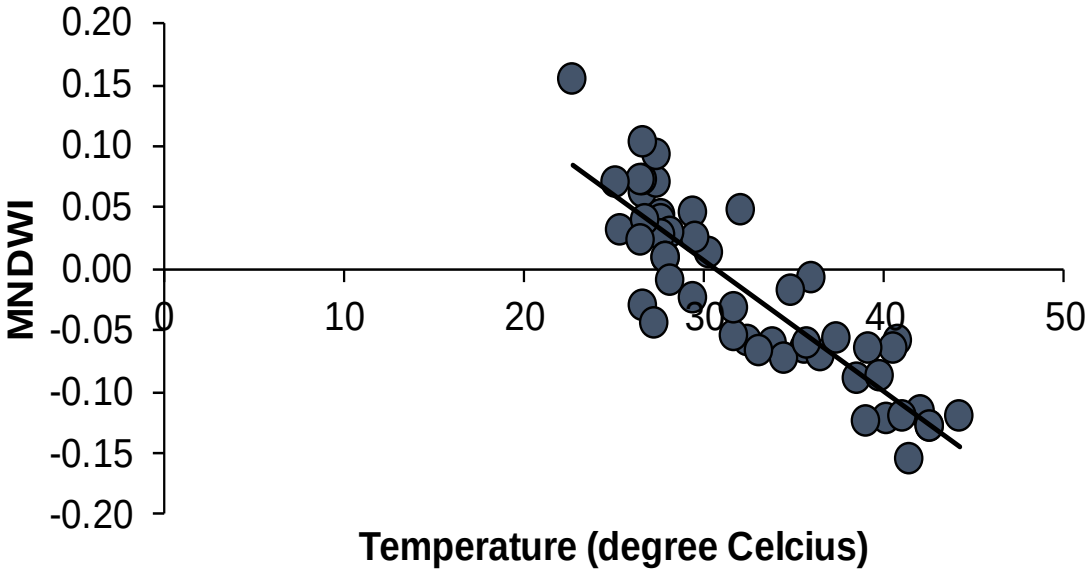


**Figure 4-12.** MNDWI and surface temperature relationship

## 4.8 Spatial and temporal variation detection using high-resolution images

Two high-resolution images secured separately by RapidEye satellite during dry and wet season of year 2014 were used to evaluate the spatial and temporal variations in lakes and rivers of Benguet catchment. During summer, the image presented clear water flowed over the tributaries in between of placer deposits. In addition, placer materials were completely dry without traces of water overflow from streams nor siltation on adjacent inland waters (**Figure 4-13A and B**). In contrast, images of wet season revealed greenish lakes. Placer materials, particularly those at the discharge outlets were washed-out and mixed with inland waters. It revealed that placer materials that were washed-out during wet season could be observed at discharge outlets. The area coverage of placer materials at this section was reduced, and iron-bearing minerals were continuously being

replaced periodically. Moreover, turbid water running throughout small streams carried small placer materials from the upstream (**Figure 4-13C**).

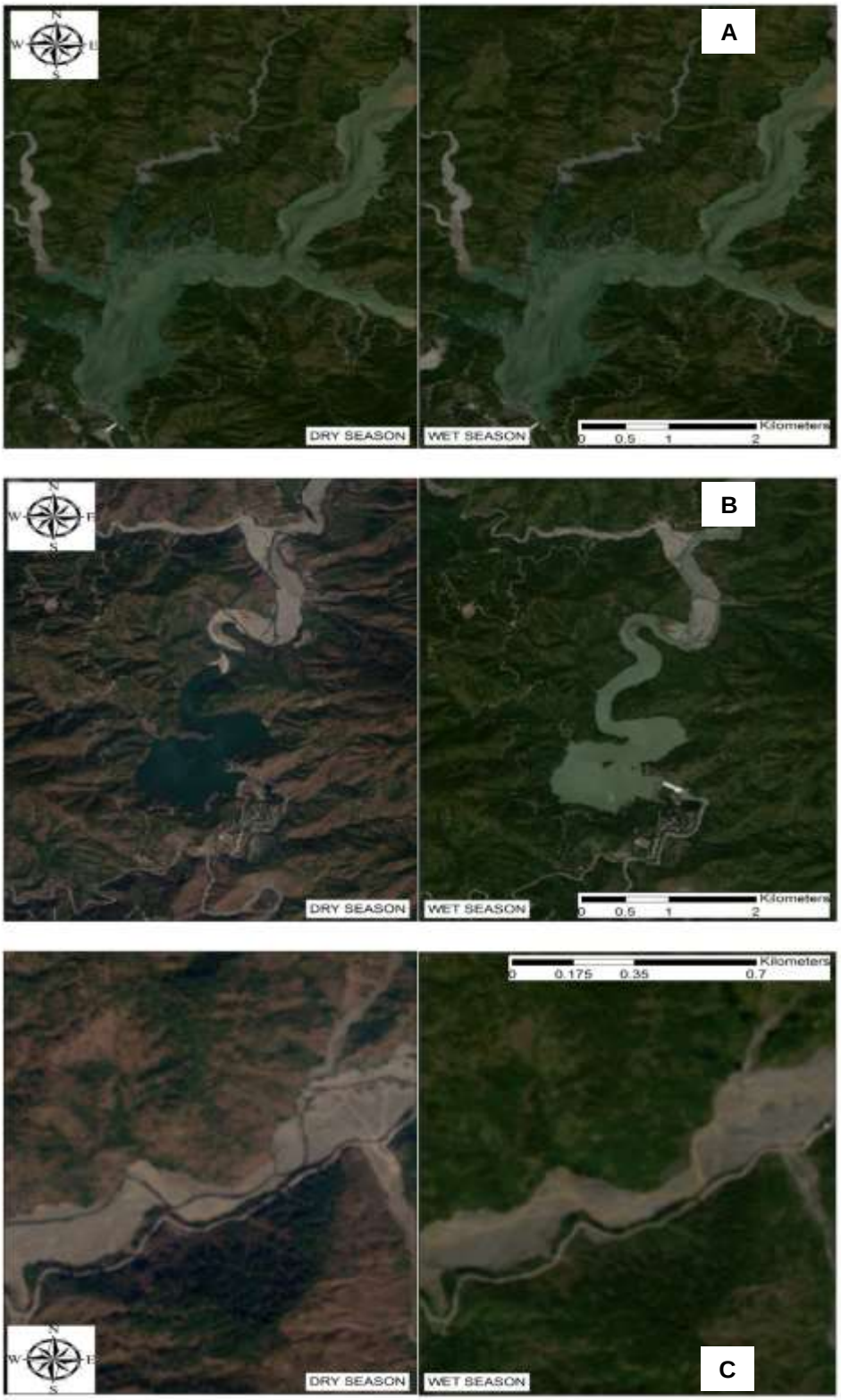


**Figure 4-13.** RapidEye images of Benguet catchment during dry and wet seasons

2014 RapidEye images courtesy of Planet Team (2018)

## 4.9 Conceptualization of an environmental monitoring program

A thematic map that presented iron-bearing minerals over the other placer materials was generated as shown in **Figure 4-14**. The relative locations of iron-bearing minerals were used as indicators for identifying environmental monitoring stations. Using the thematic map, potential locations of environmental monitoring sites were identified in consideration of the dominant topographic process of the selected sub-drainage basins. Environmental monitoring stations 1, 4, 5 and 13 were positioned over the river sections dominated by diffusive processes. Whereas stations 2 and 8 were placed over the two main discharge outlets of Ambuklao and Binga lakes. These stations could be utilized to understand the dynamics of mine-water effluent separately generated by anthropogenic activities and natural phenomena. The river sections dominated by fluvial processes could be receivers only of anthropogenic impacts from the upstream. In contrast, the upstream of the catchment was dominated by diffusive processes particularly those situated in small tributaries.

Furthermore, acquisition of TSS and Hg concentration data could be collected from these environmental monitoring stations. Afterwards, these water quality data can be used to model each sub-drainage basin driven by a particular topographic process.

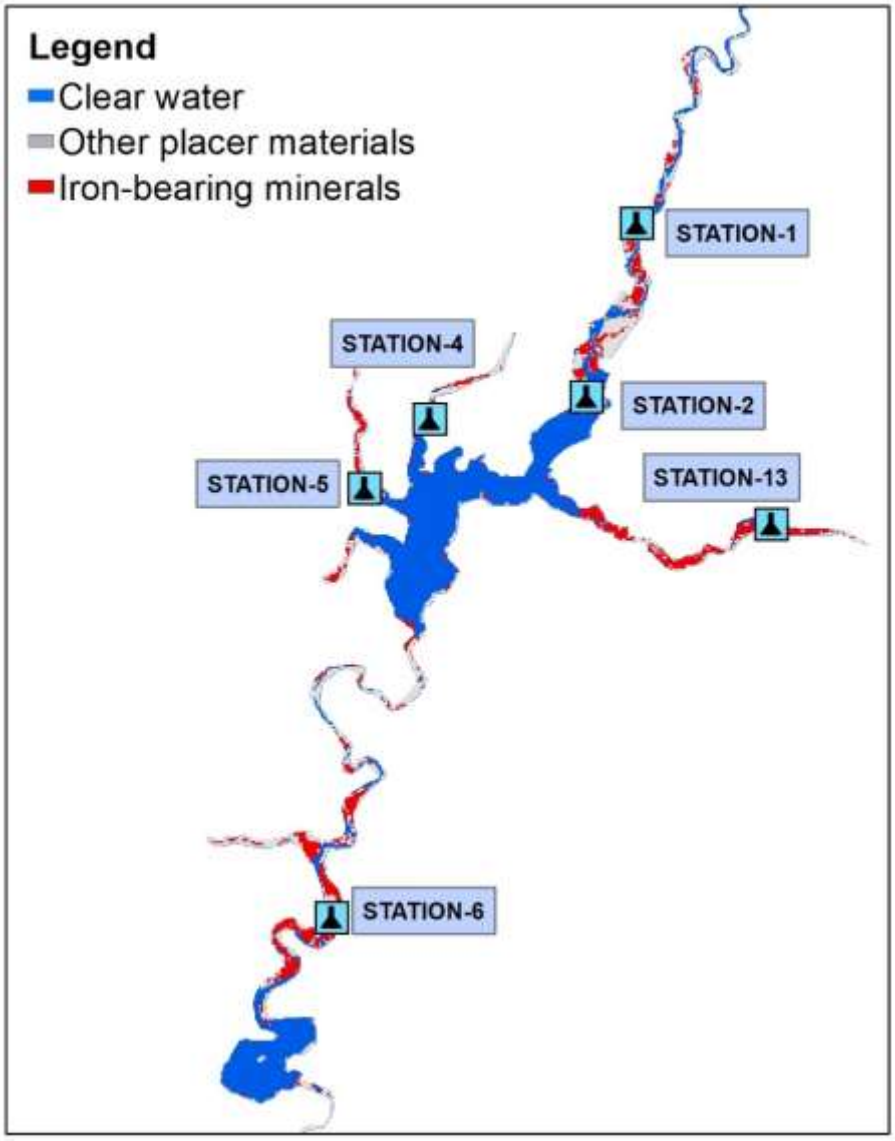


**Figure 4-14:** Proposed environmental monitoring sites for Benguet catchment

# 5. CONCLUSIONS AND RECOMMENDATIONS

## 5.1 Conclusions

In this research, selected remote sensing indices, which utilized subsections of infrared region were investigated to determine their applicability in designing an effective water quality monitoring program in placer regions. It was observed that sub-drainage basins were regulated by two different placer-forming processes namely diffusive and fluvial processes. The application of remote sensing indices allowed the identification of sub-drainage basins with which, these placer-forming processes were observable. Afterwards, environmental monitoring sites, which equally represented sections of placer deposit separately dominated by diffusive and fluvial processes, were identified to improve the water quality monitoring program in Benguet catchment.

Initially, the application of Modified Normalized Difference Water Index (MNDWI) was tested on its applicability to separate inland waters from placer deposits. Based on the results, inland waters (e.g. rivers, lakes) and placer deposits have inverse spectral response at near infrared region, and it was more evident at shortwave infrared region. It was observed that inland waters within the Benguet catchment highly absorbed shortwave infrared whereas placer deposits reflected it back to the Landsat-8 satellite OLI sensor. With the application of MNDWI, its generated thematic maps presented inland waters in Benguet catchment with positive MNDWI values as high as 0.50 whereas placer deposits resulted in negative MNDWI values as low as -0.35. In contrast, the Ferrous Mineral Ratio Index (FMR) was used to delineate sections of placer deposits with considerable level of iron-bearing minerals. Based on the generated thematic maps, placer

deposits and iron-bearing minerals almost have similar spectral signature except for the higher reflectance values of iron-bearing minerals at shortwave infrared over the near infrared compared with other placer materials. These reflectance values were associated with the iron concentration level of the minerals. However, the active weathering on mountain slopes of the catchment was succeeded by continuous replenishment of placer materials. Therefore, consistent low-grade iron minerals were perceived within the catchment. They were detected as additional area coverage during the 1st and 2nd quarters which ranges from 0.1 $km^2$ to 1.7 $km^2$.

During high rainfall season (e.g. 3$^{rd}$ quarter of the year), iron-bearing minerals were not detectable as mudflows covered placer materials near the discharge outlets while turbid water continuously flashed-out placer materials from higher elevation. Initially, this spatial phenomenon was confirmed through the observed quarterly variation in spectral signatures of selected pixels of monitoring stations. The aggregate effect of mudflow and turbid water resulted in a spectral signature with reflectance remarkably higher at the near infrared compared with the shortwave infrared. Afterwards, the presence of mudflow and turbid water in rivers was confirmed using two very-high resolution images from RapidEye captured separately in dry and wet season.

Lastly, calibrated thermal satellite images into ground surface temperature were also useful in separating these Earth features. Deep water bodies absorbed thermal infrared whereas placer deposits and shallow rivers mostly reflected thermal infrared. However, turbid water and mudflow during high rainfall season (e.g. 3$^{rd}$ quarter of the year) reduced the observed surface temperature of placer deposits. The plot of ground

surface temperature against MNDWI values presented an inverse linear relationship with an $R^2$ value of 77% and RMSE of 0.03 only. Those points below the horizontal axis represented test points located over placer deposits whereas points above the horizontal axis represented test points acquired over water bodies.

## 5.2 Recommendation for Future Work

The current research used satellite imaging, and it was restricted by the availability of both near infrared and shortwave infrared spectral bands in moderate resolution satellite sensors only such as Landsat-7 ETM+ and Landsat-8 OLI. Their spatial resolution of 30 m means that the research can be performed at regional scale.

For future applications, the thematic maps of iron-bearing minerals can be useful as substitute for detecting active anthropogenic movements in Benguet placer regions, which can assist in generating an excellent water quality monitoring program to protect watershed areas. The monitoring program can be updated quarterly, and it depends on the spatial variation detected on iron-bearing minerals. In the future, the compilation of water quality data at several monitoring stations can be valuable for water quality calibration and modelling of Benguet catchment. Afterwards, a local scale verification of the relationship between iron concentration level and reflectance at infrared region can be performed during ground survey using a spectrophotometer. In the current research, the detected reflectance at shortwave infrared region was constrained within the 30 m x 30 m spatial coverage of Landsat-8 OLI sensor, which represented aggregates of iron-bearing minerals.

# BIBLIOGRAPHY

Abdul-Wahab, S. A., & Marikar, F. A. (2011). The environmental impact of gold mines: pollution by heavy metals. *Central European Journal of Engineering, 2*, 304. doi:10.2478/s13531-011-0052-3

Alasta, A. F. (2011). Using Remote Sensing data to identify iron deposits in central western Libya. *International Conference on Emerging Trends in Computer and Image Processing*, 57-61.

Al-Fares, W. (2013). *Historical Land Use/Land Cover Classification Using Remote Sensing: A Case Study of the Euphrates River Basin in Syria.* New York: Springer.

Appleton, J. D., Williams, T. M., Breward, N., Apostol, A., Miguel, J., & Miranda, C. (1999). Mercury contamination associated with artisanal gold mining on the island of Mindanao, Philippines. *The Science of the Total Environment, 228*, 95-109. doi:10.1016/S0048-9697(99)00016-9

Aryee, B. N., Ntibery, B. K., & Atorkui, E. (2003). Trends in the small-scale mining of precious minerals in Ghana: a perspective on its environmental impact. *Journal of Cleaner Production, 11*, 131-140.

Atkinson, P. M., & Foody, G. M. (2002). Uncertainty in Remote Sensing and GIS Fundamentals. John Wiley & Sons, Ltd.

Barsi, J. A., Lee, K., Kvaran, G., Markham, B. L., & Pedelty, J. A. (2014). The Spectral Response of the Landsat-8 Operational Land Imager. *Remote sensing, 6*, 10232-10251. doi:10.3390/rs61010232

Behnam, A., Wickramasinghe, D. C., & Abdel, G. M. (2016). Automated progress monitoring system for linear infrastructure projects using satellite remote sensing. *Automation in Construction, 68*, 114–127. Retrieved from http://dx.doi.org/10.1016/j.autcon.2016.05.002

Campbell, J. B., & Wynne, R. H. (2011). *Introduction to Remote Sensing* (5th ed.). New York, United States: The Guilford Press.

Canilao, M. A. (2017). Weight of Evidence Predictive Modelling and Potential Locations of Ancient Gold Mining Settlements in Benguet in the 16th to 18th Centuries. *Philippine Journal of Science, 146*(2), 187-192.

Chander, G., Markham, B. L., & Helder, D. L. (2009). Summary of current radiometric calibration coefficients for Landsat MSS, TM, ETM+, and EO-1 ALI sensors. *Remote Sensing of Environment, 113*(5), 893-903. doi:10.1016/j.rse.2009.01.007

Chavez Jr., P. S. (1988). An Improved Dark-Object Subtraction Technique for Atmospheric Scattering Correction of Multispectral Data. *Remote sensing of Environment, 24*(459), 459-479. doi:0034-4257/88

Cohen, S., Willgoose, G., Hancock, & Greg. (2008). A methodology for calculating the spatial distribution of the area-slope equation and the hypsometric integral within a catchment. *Journal of Geophysical Research, 113*(F3), 1-13. Retrieved from https://doi.org/10.1029/2007JF000820

Cooke, D. R. (1990). The development of epithermal gold and porphyry copper-style mineralization within an intrusive center: Acupan, Baguio District, Philippines. *Pacific Rim Conference*, (pp. 521-528).

Cronan, D. S. (1980). *Underwater minerals.* Academic Press.

da Silva, B. B., Braga, A. C., & Braga, C. C. (2016). Procedures for calculation of the albedo with OLI-Landsat8 images: Application to the Brazilian semi-arid. *Revista Brasileira de Engenharia Agrícola e Ambiental, 20*(1), 3-8. Retrieved from http://dx.doi.org/10.1590/1807-1929/agriambi.v20n1p3-8

Dogan, H. M. (2012). Mineral composite assessment of Kelkit River Basin in Turkey using remote sensing. *Journal Earth System Science, 118*(6), 701-710.

Emery, W., Camps, A., & Rodriguez-Cassola, M. (2017). Introduction to Remote Sensing. In *Basic Electromagnetic Concepts and Applications to Optical Sensors* (pp. 43-83). Elsevier Inc. doi:10.1016/B978-0-12-809254-5.00002.-6

Fernandes, F, N., & Dietrich, W. E. (1997). Hillslope evolution by diffusive processes: The timescale for equilibrium adjustments. *Water Resources Research, 33*(6), 1307-1318.

Fernandez, H. E., & Damasco, F. V. (1979). Gold Deposition in the Baguio Gold District and its Relationship to Regional Geology. *Economic Geology, 74*, 1852-1868.

Garcia, M. A., & Rodriguez, F. (2013). Analysis of MODIS NDVI time series using quasi-periodic components. *Remote Sensing and Geoinformation of the Environment, 8795*, pp. 879523-1 - 879523-8. doi:10.1117/12.2027170

Ghose, M. K., & Sen, P. K. (1999). Impact on Surface Water Quality due to the Disposal of Tailings from Iron Ore Mines in India. *Journal of Scientific & Industrial Research, 58*, 699-704.

Gilmore, S., Saleem, A., & Dewan, A. (2015). Effectiveness of DOS (Dark-Object Subtraction) method and water index techniques to map wetlands in a rapidly urbanising megacity with Landsat 8 data. *CEUR Workshop Proceedings, 1323*, pp. 100-108. Brisbane.

Goward, S. N., Masek, J. G., Williams, D. L., Irons, J. R., & Thompson, R. J. (2001). The Landsat 7 mission Terrestial research and applications for the 21st century. *Remote Sensing of Environment, 78*(1-2), 3-12.

Gujar, A. R. (2007). *Heavy mineral deposit.* CSIR National Institute of Oceanography. Retrieved from http://drs.nio.org/drs/bitstream/handle/2264/759/Refresher_Course_Mar_Geol_Geophys_2007_Lecture_Notes_32.pdf;jsessionid=38636B896CB2F35087864B1320D2DBF0?sequence=2

Haneberg, W. C., Lerner, L., & Newton, D. E. (2014). *The Gale Encyclopedia of Science* (Vol. 5). Farmington Hills: Cengage Learning.

Harraz, H. Z. (2013). *Placer Mine Deposits.* doi:DOI: 10.13140/RG.2.1.3264.0886

Heylmun, E. B. (Gold in the Philippines, October 2003). Retrieved from ICMJ's Prospecting and Mining Journal: https://www.icmj.com/magazine/article/gold-in-the-philippines-1470/

Hosch, W. L. (2006). Encyclopedia Britannica. In *Geology.*

Isidro, C. M., McIntyre, N., Lechner, A. M., & Callow, I. (2017). Applicability of Earth Observation for Identifying Small-Scale Mining Footprints in a Wet Tropical Region. *Remote Sensing, 9*, 945-967. doi:10.3390/rs9090945

Kamran, K. V., Pirnazar, M., & Bansouleh, V. F. (2015). Land Surface Temperature retrieval from Landsat-8 TIRS-comparison between Split Window algorithm and SEBAL method. *Third International Conference on Remote Sensing and Geoinformation of the Environment*, (pp. 953503-1-953503-12). doi:10.1117/12.2192491

Khorram, S., Nelson, S. A., Koch, F. H., & van der Wiele, C. F. (2012). *Remote Sensing.* New York, United States of America: Springer. doi:10.1007/978-1-4614-3103-9

Kiefer, I., Odermatt, D., Anneville, O., Wuest, A., & Bouffard, D. (2015). Application of remote sensing for the optimization of in-situ sampling for monitoring of phytoplankton abundance in a large lake. *Science of the Total Environment*, 527-528. Retrieved from http://dx.doi.org/10.1016/j.scitotenv.2015.05.011

Koutsias, N., & Pleniou, M. (2015). Comparing the spectral signal of burned surfaces between Landsat 7 ETM+ and Landsat 8 OLI sensors. *International Journal of Remote Sensing, 36*(14), 3714-3732. doi:10.1080/01431161.2015.1070322

Lubrica, N. A. (2013). GIS Applicationfor Local Governance and Accountability in Environmental Protection: The Case of Bued River. *Research and Development Center, 7*(1), 52-89.

Luethje, F., Kranz, O., & Schoepfer, E. (2014). Geographic Object-Based Image Analysis Using Optical Satellite Imagery and GIS Data for the Detection of Mining Sites in the Democratic Republic of Congo. *Remote Sensing, 6*(7), 6636-6661. doi:10.3390/rs6076636

Maglambayan, V. B., Murao, S., Corpus, T. J., Sera, K., Futatsugawa, S., & Tsuji, M. (2005). Mercury Contamination Associated with Small-Scale Gold Mining in the Upper Ambalanga River, Benguet, Philippines from River Sediment Sampling., (pp. 1-11).

Makineci, H. B., & Karabork, H. (2016). Evaluation Digital Elevation Model Generated by Synthetic Aperture Radar Data. *The International Archives of the Photogrammetry, Remote Sensing and Spatial Information Sciences, XLI-B1*, 57-62. doi:10.5194

McFeeters, S. (1996). The use of Normalized Difference Water Index (NDWI) in the Delineation of Open Water Features. *International Journal of Remote Sensing*, 1425-1432.

McIntyre, J., Moore, J., & Wyche, J. (2010). *Technical Report for the DIdipio Gold-copper Project.* Melbourne, Victoria.

McMurtry. (n.d.). *Placer Deposits.* Retrieved from University of Hawaii at Manoa: http://www.soest.hawaii.edu/oceanography/courses/OCN631/placers.pdf

Murthy, Y., & Mallick, K. (1984). Interpretation of Landsat MSS Data in an Iron-ore-bearing zone in Goa, India. *Geophysical Prospecting, 32*, 282-291.

Ogashawara, I., & Bastos, V. d. (2012). A Quantitative Approach for Analyzing the Relationship between Urban Heat Islands and Land Cover. *Remotes Sensing, 4*, 3596-3618. doi:10.3390/rs4113596

Ohmori, H. (1993). Changes in the hypsometric curve through mountain building resulting from concurrent tectonics and denudation. *Geomorphology*, 263-277. doi:0169-555X/93

Perez-Pena, J. V., Azanon, J. M., Booth-Rea, G., Azor, A., & Delgado, J. (2009). Differentiating geology and tectonics using a spatial autocorrelation technique for the hypsomteric integral. *Journal of Geophysical Research, 114*, 1-15. doi:10.1029/2008JF001092

Planet Team. (2018). *Planet Application Program Interface: In Space for Life on Earth. San Francisco, CA.* Retrieved from https://api.planet.com

Plumlee, G. S. (1999). The Environmental Geology of Mineral Deposits. *United States Geological Survey*.

Rozpondek, R., Wancisiewicz, K., & Kacprzak, M. (2016). GIS in the studies of soil and water environment. *Journal of Ecological Engineering, 17*, 134-142. doi:10.12911/22998993/63476

Segal, D. (1982). Theoretical Basis for Differentiation of Ferric-Iron Bearing Minerals, Using Landsat MSS Data. *Proceedings of Symposium for Remote Sensing of Environment. 2nd Thematic Conference on Remote Sensing for Exploratory Geology*, (pp. 949-951). Fort Worth, TX.

Trinh, L. H. (2016). Application of remote sensing technique to detect and map iron oxide, clay minerals, and ferrous minerals in Thai Nguyen Province Vietnam. *Mineral Deposit Geology, 1*, 60-66. doi:10.17073/2500-0632-2016-1-60-65

Xu, H. (2006). Modificationof normalised difference water index (NDWI) to enhance open water features in remote sensing imagery. *International Journal of Remote Sensing, 27*(14), 3025-3033. doi:10.1080/01431160600589179

Xu, H. (2008). A new index for delineating built-up land features in satellite imagery. *International Journal of Remote Sensing, 29*(14), 4269-4276. Retrieved from https://doi.org/10.1080/01431160802039957